RESEARCH MEMORANDUM

for the

U. S. Air Force

ROCKET-MODEL INVESTIGATION OF THE LONGITUDINAL STABILITY,

DRAG, AND DUCT PERFORMANCE CHARACTERISTICS OF THE

NORTH AMERICAN MX-770 (X-10) MISSILE AT MACH

NUMBERS FROM 0.80 TO 1.70

By Aleck C. Bond and Andrew G. Swanson

Langley Aeronautical Laboratory
Langley Field, Va.

NATIONAL ADVISORY COMMITTEE
FOR AERONAUTICS
WASHINGTON

APR 16 1953

NASA Technical Library

3 1176 01438 5919

NATIONAL ADVISORY COMMITTEE FOR AERONAUTICS

RESEARCH MEMORANDUM

for the

U. S. Air Force

ROCKET-MODEL INVESTIGATION OF THE LONGITUDINAL STABILITY,

DRAG, AND DUCT PERFORMANCE CHARACTERISTICS OF THE

NORTH AMERICAN MX-770 (X-10) MISSILE AT MACH

NUMBERS FROM 0.80 TO 1.70

By Aleck C. Bond and Andrew G. Swanson

SUMMARY

A free-flight 0.12-scale rocket-boosted model of the North American MX-770 (X-10) missile has been tested in flight by the Pilotless Aircraft Research Division of the Langley Aeronautical Laboratory. Drag, longitudinal-stability, and duct performance data were obtained at Mach numbers from 0.8 to 1.7 covering a Reynolds number range of about 9×10^6 to 24×10^6 based on wing mean aerodynamic chord.

The lift-curve slope, static stability, and damping-in-pitch derivatives showed similar variations with Mach number, the parameters increasing from subsonic values in the transonic region and decreasing in the supersonic region. The variations were for the most part fairly smooth. The aerodynamic center of the configuration shifted rearward in the transonic region and moved forward gradually in the supersonic region. The pitching effectiveness of the canard control surfaces was maintained throughout the flight speed range, the supersonic values being somewhat greater than the subsonic. Trim values of angle of attack and lift coefficient changed abruptly in the transonic region, the change being associated with variations in the out-of-trim pitching moment, control effectiveness, and aerodynamic-center travel in this speed range. Duct total-pressure recovery decreased with increase in free-stream Mach number and the values were somewhat less than normal-shock recovery. Minimum drag data indicated a supersonic drag coefficient about twice the subsonic drag coefficient and a drag-rise Mach number of approximately 0.90. Base drag was small subsonically but was about 25 percent of the minimum drag of the configuration supersonically.

Comparison of the flight data with existing wind-tunnel data for the same configuration in general showed fair to good agreement. The greatest differences between the flight and tunnel data were noted in the lift-curve slopes, and it was shown that the major portions of these differences resulted from aeroelastic effects on the wing and flexibility effects of the fuselage of the flight model.

INTRODUCTION

An investigation of the drag, longitudinal stability, and duct performance characteristics of 0.12-scale models of the North American MX-770 missile project at transonic and supersonic speeds is being conducted at the present time at the Langley Pilotless Aircraft Research Station at Wallops Island, Va. at the request of the Wright Air Development Center, U. S. Air Force. Flight test of the X-10 missile, a turbojet-powered interim missile or research test vehicle of the MX-770 program, constitutes the first phase of the investigation. The second phase includes the flight test of the XSSM-A-4 or NAVAHO II missile which is a long-range, ground-to-ground, ram-jet-powered missile designed to cruise at a high supersonic Mach number.

The North American X-10 missile is a pilotless, turbojet-powered, canard configuration with twin side inlets and modified delta lifting surfaces and is designed to fly at transonic and supersonic speeds up to $M = 1.80$. The purpose of the flight test was to obtain aerodynamic data at Reynolds numbers and speeds comparable to full scale, which will aid in understanding the aerodynamic and flight characteristics of the full-scale missile.

The basic aerodynamic parameters of the configuration were obtained by analysis of the dynamic response of the model to programmed pulses of the canard control surfaces and are presented over a Mach number range from 0.80 to 1.70 and a Reynolds number range from 9×10^6 to 24×10^6, based on wing mean aerodynamic chord.

SYMBOLS

a_l acceleration along reference axis as obtained from accelerometer, positive forward, ft/sec^2

a_n acceleration normal to reference axis as obtained from accelerometer, ft/sec^2

g acceleration due to gravity, ft/sec^2

S   wing area (including area enclosed within the fuselage), sq ft

W   model weight, lb

C_C chord-force coefficient, $-\dfrac{a_l}{g}\dfrac{W}{qS}$

C_N normal-force coefficient, $\dfrac{a_n}{g}\dfrac{W}{qS}$

C_D total drag coefficient, $C_C \cos\alpha + C_N \sin\alpha$

C_L lift coefficient, $C_N \cos\alpha - C_C \sin\alpha$

$C_{D_{min}}$ total minimum drag coefficient of configuration

C_{D_i} total internal-drag coefficient, $\dfrac{2}{qS}\left[m(V_O - V_x) + (p_O - p_x)A_x\right]$

C_{D_B} base drag coefficient, based on wing area

C_m pitching-moment coefficient about model center of gravity, based on wing area and wing mean aerodynamic chord

C_{m_O} pitching-moment coefficient at zero lift and zero canard deflection

C_p base pressure coefficient, $\dfrac{p_b - p_O}{q}$

p_b base pressure, lb/sq ft

p   static pressure, lb/sq ft

q   free-stream dynamic pressure, $\dfrac{\gamma}{2}p_O M_O^2$, lb/sq ft

M   Mach number

V   velocity, ft/sec

V_c velocity of sound, ft/sec

R   Reynolds number, based on wing mean aerodynamic chord

P   period of pitching oscillations, sec

t   time, sec

$t_{1/2}$ time for pitching oscillations to damp to one-half
amplitude, sec

b   wing span, ft

$\bar{c}$ wing mean aerodynamic chord, ft

y   lateral distance from center line of model, ft

A   area, sq ft

H   total pressure, lb/sq ft

m   mass flow through one duct, slugs/sec

m_0 mass flow through a stream tube of area equal to inlet area
of one duct under free-stream conditions, slugs/sec

α angle of attack of reference axis, deg

α_0 angle of attack at zero lift and zero canard deflection, deg

δ angle between fuselage axis and canard chord measured in the
plane of symmetry of the model, positive trailing edge
down, deg

θ angle of pitch, radians

ϕ local wing twist angle produced by unit load applied perpendicular to wing chord at 50-percent chord line, positive
leading edge up, radians/lb

γ ratio of specific heats (1.40)

Subscripts:

T   trim

o   free-stream condition

i   condition at duct inlet

x   condition at duct exit

SL   sea-level standard condition (59° F and 2116 lb/sq ft)

D   condition in duct

$$\dot{\alpha} = \frac{1}{57.3} \frac{d\alpha}{dt} \frac{\bar{c}}{2V}$$

$$q = \frac{d\theta}{dt} \frac{\bar{c}}{2V}$$

The symbols α, $\dot{\alpha}$, δ, and q used as subscripts denote the partial derivative of the quantity with respect to the subscript; for example, $C_{m_\alpha} = \frac{\partial C_m}{\partial \alpha}$.

MODEL AND APPARATUS

A 0.12-scale model of the North American MX-770 (X-10) missile was used in the investigation. A sketch of this model is shown in figure 1 and photographs are shown as figure 2. The wing of the model was a modified 60° delta with the tips raked inward 30° resulting in an aspect ratio of 1.87. The wing was mounted on the lower part of the fuselage at 2° negative incidence to the fuselage reference line. The wing utilized a modified NACA 66-series airfoil section in the free-stream direction with a 2.83-percent thickness at the root chord (wing station zero) and a 6-percent thickness at the 87.26-percent semispan. Ordinates for sections at the 0- and 87.26-percent semispan stations are given in table I.

The canard control surfaces were geometrically similar in plan form to the wing but had 15° dihedral. A modified NACA 66-series airfoil section in the free-stream direction was utilized with a constant 5-percent-thickness ratio. Ordinates for the canard are given in table II. The axis of rotation was located at the 50.6-percent station of the canard mean aerodynamic chord.

The model had two vertical-tail surfaces of modified biconvex airfoil section, approximately 5 percent thick, mounted on the engine nacelles and displaced 25° outward from vertical. Ordinates for the tail surfaces are given in table III.

The model was equipped with twin sharp-lipped normal-shock-type side inlets with boundary-layer bleeds located forward of the entrance lip. The duct inlets were of nearly circular cross section and the interior duct lines simulated the full-scale ducts from the inlet lip to the section of maximum duct area. Rearward from this point, a transition was made to a circular cylinder which continued to the exit nozzle.

The measured inlet areas of the left and right ducts were 6.10 square
inches and 6.14 square inches, respectively. The boundary-layer bleeds
located 0.91 inch ahead of the inlets were 0.26 inch in height and had
measured areas of 0.75 square inch each. The boundary-layer mass flow
was ducted to the free stream through three diverging passages, two of
which exhausted on the upper side of the inlet and one exhausted on the
lower side of the inlet. Details of the inlet and boundary-layer bleed
system may be seen in figure 3. The mass flow through the ducts was
controlled by the duct exit nozzles which were designed to simulate the
estimated full-scale mass-flow ratio at the peak Mach number. The exit
nozzle was a simple convergent nozzle with a minimum diameter of 2.55 inches
which gave a nozzle contraction ratio of 0.406. A view of the after end
of the model showing the duct exits is shown in figure 4.

The basic body of the model was composed of a parabolic forebody
and a cylindrical center section. The afterbody faired into the duct
and wing lines as shown in figures 1, 2, and 3.

The model was constructed essentially of the following materials:
wing, magnesium plate; canards, steel; vertical tails, aluminum-alloy
casting; forward body, magnesium sheet; afterbody, magnesium casting;
duct inlets, aluminum alloy.

The canard control surfaces were pulsed by a hydraulic servosystem
in a square-wave motion from approximately -1.0° to -4.8°. The pulse
rate of the canards was changed during the flight by means of a pressure-
operated switch at a predetermined value of free-stream total pressure.

The model weighed 156.15 pounds and the moment of inertia in pitch
was 20.39 slug-feet^2. The center of gravity of the model was at sta-
tion 56.98 or at -12.32 percent of the mean aerodynamic chord; this
value corresponded to the mean of the center-of-gravity range of the
full-scale missile. The vertical location of the center of gravity was
0.622 inch below the fuselage reference line.

                              INSTRUMENTATION

The model was equipped with a telemeter system which transmitted
12 channels of information of which 8 channels were continuous and
4 channels were switched. The eight continuous channels of information
were longitudinal acceleration (high and low range), normal accelera-
tion (high and low range), angle of attack, canard position, and two
base pressures. The switched channels transmitted external total pres-
sure, duct total pressure, duct nozzle static pressure, and a reference
static pressure (included solely for use in determining flight Mach num-
ber in the event of failure of tracking radar). The accelerometers were

mounted as near the center of gravity of the model as practical in order
to keep the accelerometer corrections to a minimum. Angle of attack was
measured by means of a vane-type instrument (ref. 1) located on a sting
ahead of the nose of the model (fig. 1). The two base pressure measure-
ments were of (1) the pressure at essentially the center of the base and
(2) the average pressure of four manifolded pressure orifices equally
spaced about the exit of the left duct. Locations of the base-pressure
orifices are shown in figure 5. The external total pressure was measured
by a total-pressure tube located on a small strut below the fuselage, as
shown in figure 1. The reference static pressure measured was the pres-
sure inside the cone of the angle-of-attack vane. The duct total pres-
sure was measured just ahead of the exit nozzle by a six-tube manifolded
total pressure rake as shown in figure 5. The pressure rake was inclined
at an angle of $35°$ to the lateral axis of the model and the tubes were
positioned on an equal area basis. An orifice located in the minimum
section of the exit nozzle as shown in figure 5 was used to measure the
duct nozzle static pressure.

A CW Doppler radar unit was used for obtaining checks on the model
velocity and a tracking radar unit was employed for obtaining the model
range, elevation and azimuth as a function of time. Atmospheric condi-
tions were determined from a radiosonde released at the time of firing.
Fixed and manually operated 16-millimeter, 35-millimeter, and 70-millimeter
cameras were employed to record the launching and initial portion of the
flight test.

TEST AND ANALYSIS PROCEDURES

Test

The model-booster combination was ground-launched at an angle of
$55°$ from the horizontal from a mobile-type launcher as shown in figure 6.
The model was boosted to a peak Mach number of 1.70 by a single-stage
booster utilizing two 6-inch solid-fuel ABL Deacon rocket motors. By
virture of its lower drag to weight ratio, the model separated from the
booster at rocket burnout. The model had no sustaining rocket motor and
hence experienced decelerating flight after separation from the booster.

The Reynolds numbers (based on the wing mean aerodynamic chord)
obtained during the flight test are shown in figure 7 as a function of
Mach number. Plots of the ratios $\dfrac{V_c}{V_{c_{SL}}}$ and $\dfrac{p_o}{p_{o_{SL}}}$ for the flight are
presented in figure 8.

The data on the characteristics of the model were obtained during
the decelerating portion of the flight. The model was disturbed in pitch
by a programmed variation of the canards in an approximate square wave
pattern. The controls were set to operate between the limits of -4.8°
and -1.0° at a rate of 1 cycle in 1.7 seconds during the supersonic por-
tion of the flight (from separation to $M \approx 1$) and at a rate of 1 cycle
in 3.1 seconds during the subsonic portion of flight. During the flight,
the control position indicator showed that the canard remained at a fixed
deflection after each pulse, but the deflection angles for both the high
and low deflections after each pulse varied somewhat from the preset
stop values. The incremental change in deflection for each pulse, how-
ever, remained essentially constant. A time-history of the canard deflec-
tion angle and Mach number is shown in figure 9. Behavior of the canard
deflection in this manner indicates that the control position indicator
or pulsing mechanism (or both) was being affected by the aerodynamic and
inertial loading of the system in the longitudinal direction rather than
in the normal direction. Play or flexibility in the various components
of the system of approximately 0.025 inch would be sufficient to cause
the observed shifts in stop position. Ground tests with an identical
control system in an identical model failed to disclose any conclusive
evidence as to the exact cause of the shifts. Since the canard deflec-
tion was constant after each pulse, the character of resulting oscilla-
tions was not changed, and hence the stability and damping data were not
affected; however, the trim data may be less accurate due to the possible
introduction of error in the value of the canard deflection angle.

Analysis

The model velocity and free-stream conditions were determined by
using radiosonde, tracking radar, and external total-pressure data. The
Doppler radar obtained velocity data during the boost period, but failed
to track the model immediately after separation, giving only intermittent
velocity data; hence, these data were used where available to serve as a
check on the model velocity.

The angles of attack measured by the vane on the nose of the model
were corrected to angles of attack at the model center of gravity by the
method of reference 1.

The short-period longitudinal oscillations resulting from deflec-
tion of the canards were analyzed by the method of reference 2 to obtain
the trim, static and longitudinal stability, and lift characteristics of
the model. Since the trim data were obtained for different values of δ
for each pulse, the values of $\left(\dfrac{\Delta\alpha}{\Delta\delta}\right)_{trim}$ and $\left(\dfrac{\Delta C_L}{\Delta\delta}\right)_{trim}$ were calculated

by using the corresponding trim values at the end of a given pulse and beginning of the succeeding pulse. With the use of the calculated values, the trim characteristics at constant δ and the control effectiveness characteristics were calculated.

The base drag on the model was calculated by using the assumption that the base pressure measured by the manifolded pressure orifices was the average pressure over the annular base areas about the two duct exits and that the center base pressure measurement was the average pressure over the remainder of the base area. A sketch of the base of the model is shown in figure 5 illustrating the assumed proportioning of the base area.

The duct total-pressure recovery was obtained from a comparison of the measured duct total pressure with the free-stream total pressure. The mass-flow ratio was calculated using the relation

$$\frac{m}{m_O} = \frac{A_X}{A_1} \frac{p_X}{p_O} \frac{M_X}{M_O} \left[\frac{1 + \dfrac{\gamma - 1}{2} M_X{}^2}{1 + \dfrac{\gamma - 1}{2} M_O{}^2} \right]^{1/2}$$

The ratio of measured nozzle exit static pressure to duct total pressure was used to indicate the transition from sonic to subsonic flow in the nozzle exit. The value of M_X was taken equal to 1.0 where the pressure ratio indicated sonic flow, whereas for subsonic flow, the value of M_X was determined directly from the pressure ratio. By assuming $H_X = H_D$, the value of p_X was determined from the pressure ratio p_X/H_X compatible with the value of M_X. The internal duct drag was calculated by considering the momentum and pressure differences in the entering stream tube from free stream to the duct exit and is represented by the expression

$$D = m(V_O - V_X) + (p_O - p_X)A_X$$

where the average value of V_X was used computed by means of one-dimensional compressible-flow theory.

The effects of wing flexibility on model lift-curve slope were determined by means of the method of reference 3 by using wing flexural properties (fig. 10) determined from a wing geometrically similar and constructed of the same material as the wing of the flight model. The span loading employed was obtained from reference 4. Distribution of

model lift was determined from the data of reference 5 and information contained in reference 6. Wing inertia effects were neglected in these calculations.

The effect of fuselage flexibility on the indicated angle of attack was estimated by determining the angular deviation of the nose of the model due to a given loading condition encountered in the flight. The aerodynamic loading was estimated by using the information of reference 6 and the inertia loading was calculated from flight data by using weight distributions of reference 7. The deflection of the fuselage was estimated by using unpublished fuselage static deflection data from tests made by North American on the flight model.

Accuracy

Possible systematic errors in the absolute level of directly measured quantities are proportional to the total range of the measuring instruments. On the basis of statistical data compiled by the Instrument Research Division of the Langley Aeronautical Laboratory, it is believed that the instrumentation of this model was accurate to within ± 1 percent of the full-scale range for pressure measuring instruments and $\pm 1\frac{1}{2}$ percent for the remaining instruments. Coefficients calculated from these directly measured quantities are subject to further errors resulting from possible inaccuracies in determination of atmospheric properties and model space position. For the flight ranges of this model, it is believed that combined errors of tracking radar and radiosonde data would result in possible errors of not more than ± 1 percent of measured values of ambient pressure and temperature at the recorded altitude of the model if it is assumed that the atmospheric conditions encountered by the model are the same as those determined by the radiosonde.

Based on the aforementioned values, possible errors in the absolute values of quantities are as follows:

M	ΔM	ΔC_N	ΔC_C	ΔC_p	$\Delta \frac{H_D}{H_O}$	$\Delta \alpha$	$\Delta \delta$
1.7	± 0.01	± 0.002	± 0.002	± 0.01	± 0.015	± 0.45	± 0.06
1.2	$\pm .02$	$\pm .008$	$\pm .003$	$\pm .04$	$\pm .040$	$\pm .45$	$\pm .06$
.8	$\pm .04$	$\pm .016$	$\pm .004$	$\pm .07$	$\pm .075$	$\pm .45$	$\pm .06$

These errors, systematic in nature, are dependent on radar and telemeter precision; therefore, relative values and parameters dependent upon slopes of measured quantities are, in general, more accurate than

the foregoing would indicate. Derivatives, such as $C_{m_q} + C_{m_{\dot{\alpha}}}$ and C_{L_δ}, determined from mathematical relations of measured quantities, are of more questionable accuracy. Since the value of C_{m_α} is dependent to a greater extent on the period of oscillation, an approximation of the order of accuracy of this parameter may be determined from the scatter in the period data.

The angle-of-attack data are subject to an additional possible error of $\pm 0.5^\circ$ due to asymmetries, which may cause the vane to trim at angles to the airstream, and friction in the vane pivot, which may cause hysteresis loops in parameters varying with angle of attack. As mentioned in the section entitled "Test," there is an additional possible uncertainty in the canard deflection angle which could result in inaccuracies in the absolute level of trim data calculated at constant δ.

Single data points are subject to further inaccuracies due primarily to errors in reading the film records of the telemetered data. On the basis of statistical studies, approximately 90 percent of the points read should have an error of less than ± 1 percent (based on full-scale instrument range). These errors are random in nature and should be virtually eliminated in the final analysis by judicious fairing of the scatter in the test data points.

A discussion of some of the effects on accuracy of assumptions made in determining model characteristics by the pulse control technique, including neglected terms, acceleration effects, and effects of nonlinearities, is given in the appendixes of reference 2.

RESULTS AND DISCUSSION

Lift

Plots of variation of lift coefficient with angle of attack for the first one or two oscillations following a control pulse are presented in figure 11. The Mach number variation during these cycles was of the order of 0.03, the Mach number shown on the figure being the average for the data presented. The data for $M = 0.89$ are used for a portion of only 1 cycle due to excessive scatter in the data for the remainder of the oscillations for that pulse. The difference in C_L between increasing α and decreasing α probably results primarily from an angle-of-attack lag caused by friction in the vane system as mentioned in the section "Accuracy." Slopes do not appear to be appreciably affected by this displacement except near the peaks of the oscillations. The lift curves appear to be fairly linear within the angle-of-attack range covered, departures from linearity resulting, it is believed, from scatter in the experimental data.

Variation of lift-curve slope with Mach number as obtained from the lift plots is presented in figure 12. No significant variation was noted between data points at high and low canard deflection angles. The lift-curve slope increased from the subsonic value to a peak at $M = 1.05$ and then decreased smoothly with increase in Mach number.

Values of lift-curve slope from the wind-tunnel data of reference 5 and the curve from reference 6 for the same configuration as reported herein are also presented in figure 12 for comparison. The values measured in free flight were of the order of 10 percent lower than the wind-tunnel data of reference 5. It is believed that these differences are due largely to the differences in flexibility of the components of the two models and the differences in the dynamic pressures of the tests. The effect of wing aeroelasticity on the model lift-curve slope was estimated as stated in the section "Analysis" for Mach numbers from 1.2 to 1.7. This effect is shown in figure 12 as a reduction in C_{L_α} due to wing aeroelasticity and is a relatively small quantity over this speed range. The estimated effect of fuselage flexibility on the measured values of C_{L_α}, also presented in figure 12, was calculated at $M = 1.55$ only and is of the order of two and one-half times the magnitude of the wing aeroelastic effect for the one point calculated. This correction of the effect of fuselage flexibility on measured C_{L_α} will decrease as Mach number decreases. The total C_{L_α} of the model, including wing aeroelastic and fuselage flexibility effects, is presented in figure 12 at $M = 1.55$. This value shows closer correlation with the wind-tunnel data and hence justifies the belief that the observed differences between the wind-tunnel and flight data were due largely to differences in flexibility of the components of the respective models. Measured values of C_{L_α} were used in the calculation of all parameters involving the use of C_{L_α}.

Static Stability

The measured periods of pitch oscillation of the model, a measure of static stability, are presented in figure 13 as a function of Mach number. It is noted that there is no marked difference in the period as determined at the high or low control deflections. These period data were used to calculate the static-stability derivative C_{m_α} which is presented in figure 14. Values of C_{m_α} increased negatively from the value at $M = 0.80$ to a peak at $M = 1.05$ and then decreased gradually with increase in Mach number.

Using the values of C_{L_α} and C_{m_α} presented in figures 12 and 14, respectively, the aerodynamic-center location was determined and is shown in figure 15. The aerodynamic center shifts rearward approximately

16 percent $\bar{c}$ at transonic speeds from 8.5 percent $\bar{c}$ to 24.5 per-
cent $\bar{c}$. In the supersonic Mach number range, the aerodynamic center
moves rearward slightly at $M = 1.3$ and then moves forward gradually to
19.2 percent $\bar{c}$ at $M = 1.65$. The aerodynamic center derived from the
wind-tunnel data of reference 5 is included in figure 15 for purposes of
comparison. These data show close agreement with the flight data. The
curve of aerodynamic center from reference 6, also included in figure 15,
does not agree as well with the flight data and indicates a more forward
aerodynamic center; however, the trends of the two curves are quite
similar.

Dynamic Stability

Dynamic-stability data were derived from the analysis of the damping
of the short-period oscillation induced by the abrupt control deflection.
Time to damp to one-half amplitude, determined from plots of amplitude
ratios obtained from envelopes of the oscillation data, is shown in fig-
ure 16 as a function of Mach number. Data for the high control position
show no significant variation from the data for the low control position.
The values of the damping-in-pitch derivative $C_{m_q} + C_{m_{\dot{\alpha}}}$ determined from
the $t_{1/2}$ data and the C_{L_α} data of figure 12, are presented in fig-
ure 17. The value of the damping-in-pitch derivative increased negatively
in going from subsonic to supersonic speeds up to $M = 1.20$. Above
$M = 1.20$, the value of $C_{m_q} + C_{m_{\dot{\alpha}}}$ decreased gradually in absolute magni-
tude. In addition to the experimental damping curve, the calculated
damping curve for this configuration obtained from reference 8 is also
included in figure 17. It is noted that, even though the calculated
damping is considerably less than the experimental curve, the trend of
the two curves with Mach number is quite similar.

The period and time to damp to one-half amplitude presented herein
are, of course, not directly applicable to the full-scale missile, since
the test model was not dynamically similar to the full-scale missile and
since the flight conditions are not necessarily the same. The period and
damping of the longitudinal oscillation for the full-scale missile with
the same center-of-gravity location as the model may be calculated by
using the data presented herein and the physical characteristics of the
full-scale missile and model.

Longitudinal Control Effectiveness and Trim

The control derivatives C_{m_δ} and C_{L_δ} are presented in figures 18
and 19, respectively. The values of C_{m_δ} increase in the speed range
from $M = 0.8$ to $M = 1.05$, decrease slightly in the range from $M = 1.05$

to M = 1.20, and remain essentially constant thereafter. Also presented in figure 18 are the C_{m_δ} data obtained from the wind-tunnel tests of reference 5 and the curve of reference 6. The data of reference 5 show good agreement with the flight-model data over the range of speeds covered in these tests. The curve of reference 6 does not agree as well with the flight data with regard to the values, but the trend of the curve is quite similar in the lower speed range. The lift due to canard deflection C_{L_δ} was essentially zero throughout the test range, as also indicated by the data of reference 5.

The variation of trim angle of attack and trim lift coefficient with Mach number as obtained from the flight test is presented in figure 20. Since the canard deflection limits were not consistent during the test, the measured values are included on the figures. The variations with Mach number of trim angle of attack per unit control deflection and trim lift coefficient per unit control deflection are presented in figure 21; the variations are smooth and indicate minimum values near M = 1.05. Using the aforementioned data, the trim angle of attack and trim lift coefficient were calculated for a constant δ of -5°, the curves of which are presented in figure 22. The trim lift curve for δ = -5° and center of gravity at station 56.4 (-14.5 percent $\bar{c}$) reported in reference 6 is included in figure 22(b) for comparison. The data show reasonably good agreement. These trim data indicate an abrupt and rather severe trim change in both lift coefficient and angle of attack between M = 0.90 and M = 1.00. This trim change is associated with the variations in out-of-trim pitching moment, change in control effectiveness, and center-of-pressure travel which occur in this speed range.

The variation of C_{m_0} with Mach number is presented in figure 23, the values of which were calculated from the following expression derived from the conventional moment equation:

$$C_{m_0} = \frac{-C_{m_\alpha}}{C_{L_\alpha}}\left(C_{L_T}\right)_{\delta=0}$$

The flight data are compared with the wind-tunnel data of reference 5 and the curve of reference 6 and show fair agreement as to order of magnitude and trends with Mach number. The data indicate a sharp increase in C_{m_0} between the Mach numbers of 0.9 and 1.0. The angle of

attack for zero lift and zero control deflection α_0 was calculated by means of an expression derived from the lift equation of the model as

$$\alpha_0 = \left(\alpha_T\right)_{\delta=0} - \frac{\left(C_{L_T}\right)_{\delta=0}}{C_{L_\alpha}}$$

and is presented in figure 24. In the supersonic region, the level of the flight data is of the order of 0.50° higher than the wind-tunnel data of reference 5 and α_0 plot of reference 6. This may be the result of some out of trim of the vane, as noted in the section "Accuracy." The data are in good agreement in the transonic and subsonic regions and the trends with Mach number are quite similar throughout the test range. The variation of α_0 with Mach number is similar to that of C_{m_0}.

Duct Performance

Duct-performance data are presented in figure 25 as functions of Mach number. The total-pressure recovery, measured at station 86.75 in the left duct of the model is presented in figure 25(a). A comparison of the measured total-pressure recovery with the normal-shock recoveries indicates losses of the order of 7 percent at $M = 1.7$ and 2 percent at $M = 1.0$ over normal-shock losses. Results of an experimental investigation of the performance characteristics of an inlet similar to that employed on the flight model are reported in reference 9. It is pointed out in this reference that the major portion of the losses occurring at the inlet are due to the high Mach numbers which were found to exist at the inlet. In addition, some losses were attributed to flow separation of the inlet. Total-pressure values reported in reference 9 for $M = 1.5$ and $M = 1.8$ and for corresponding mass flows are included in figure 25(a). These values of recovery agree quite well with the flight data. A plot of the ratio of nozzle static pressure to duct total pressure is presented in figure 25(b). This plot indicates that the exit nozzle was choked for all free-stream Mach numbers greater than 0.98 and the value of M_X used for calculation of the mass-flow ratio was taken equal to 1.0 over this speed range. The plot of the mass-flow ratio (fig. 25(c)) shows the mass flow increasing with Mach number; the maximum value closely simulates the estimated full-scale mass-flow ratio of 0.88 at $M = 1.7$ shown in reference 6. The internal duct drag (fig. 25(d)) increases gradually in the Mach number range from $M = 1.0$ to $M = 1.7$. The values of the internal drag are quite small in comparison with the total model drag, as shown subsequently. It was assumed that conditions in both ducts were the same, and the internal drag of the instrumented duct was doubled in order to arrive at the total internal drag of the model.

For the angle-of-attack range covered in the flight test, it was not possible to make any reasonable correlation of the variation of duct total-pressure recovery with angle of attack. The data indicated some small variations of total pressure with angle of attack; however, the variations were not consistent and were generally of the order of accuracy of the measuring instrument.

Base Pressure

The size of the duct exits of the flight model was determined by consideration of the duct mass-flow requirements, and hence did not simulate the full-scale duct exits. It therefore follows that the base area of the model did not simulate the base area of the full-scale missile, thereby necessitating measurement of the model base pressures for the evaluation of full-scale drag values. Base pressure coefficients for the center orifice and manifolded orifice locations are presented in figure 26. These data show that the pressures about the duct exit were considerably lower than the pressures at the center of the base, especially during the supersonic portion of the flight. This effect is probably due to the influence of the flow issuing from the duct exit as well as the influence due to the external flow. The influence of flow issuing from a duct on base pressure is evidenced by the results of Cortright and Schroeder reported in reference 10. Their results have shown that the base pressures about an operating duct exit are reduced considerably from the power-off (no flow) values for certain low ranges of jet pressure ratio H_x/p_0. The jet pressure ratios of the flight model varied from approximately 1.90 to 3.90 in the speed range from $M = 1.0$ to $M = 1.7$ and are well within the range of pressure ratios for reduced base pressure. Presumably, the pressures at the center of the base are affected only slightly by the duct flow due to the further displacement of the center orifice from the duct exit, and hence are probably of the same order of magnitude as would be obtained in a power-off condition.

Drag

Drag polars of the total drag are plotted in figure 27 for various average free-stream Mach numbers. Using the drag polars and extrapolations thereof, the minimum drag coefficient for the configuration (including base and internal drag) was determined; the minimum drag being taken at zero lift. The minimum drag coefficient, base-drag coefficient, and internal-drag coefficient are presented in figure 28 as functions of Mach number. Values of trim drag coefficient, obtained from plots of C_D against time, were used to complete the minimum-drag curve in the transonic region and to determine the drag-rise Mach number. This was considered valid, since the trim lift of the model was reasonably low

during this interval. The drag-rise Mach number determined in this
manner is approximately 0.90. Minimum drag coefficient determined for
high and low control deflection is indicated by use of different symbols
in figure 28; no appreciable variation in the values of drag are noted
for the two control positions. The base drag coefficient curve was calcu-
lated as stated in the section "Analysis" using the base pressure coeffi-
cients of figure 26. This curve indicates very low base drag during the
subsonic portion of flight and relatively high base drag (about 25 per-
cent of minimum drag) during the supersonic portion. There is a slight
dip in the curve at $M = 0.95$, and then the base drag begins to rise to
a maximum at $M = 1.36$ and decreases gradually thereafter. The high
base drag of the model is, of course, primarily due to the large base
area of the model. The base drag coefficients of the full-scale missile
would not be expected to be as high as presented herein, since on the
full-scale missile the duct exit areas would comprise a greater percentage
of the total base area than did the duct exit areas of the flight model.
The curve of internal-drag coefficient, originally presented in fig-
ure 25(d), is repeated in order to illustrate more clearly its small
magnitude relative to the base and minimum drag coefficients. Also
plotted in figure 28 is a curve of $C_{D_{min}}$ less base- and internal-drag
coefficients with two points from the wind-tunnel data of reference 5
shown for comparison. The wind-tunnel data have been corrected to zero
base drag, but include the internal drag of the ducts; however, the
internal drag of the wind-tunnel model should be of the same order of
magnitude as that of the flight model, since the mass-flow ratios were
approximately the same. The agreement between the wind-tunnel and
flight data is considered excellent and indicates negligible scale
effect between the Reynolds numbers of approximately 20×10^6 (based
on $\bar{c}$) of the flight-test data and 5×10^6 of the wind-tunnel data.

Because of the low range of lift coefficients obtained during the
test, the induced drag factor dC_D/dC_L^2 and $(L/D)_{max}$ could not be
precisely determined. The data indicated that dC_D/dC_L^2 was of the
order of $\dfrac{1}{57.3}\, C_{L\alpha}$.

CONCLUDING REMARKS

A free-flight 0.12-scale rocket-boosted model of the North American
MX-770 (X-10) missile has been flown at Mach numbers from 0.80 to 1.70.
Data from the test indicate the following:

1. Lift-curve slope and static-stability parameter C_{m_α} varied smoothly with Mach number. The values increased from the subsonic values to a peak at a Mach number of 1.05 and then decreased gradually with increasing Mach number. The aerodynamic center shifted rearward from about 8-percent $\bar{c}$ at $M = 0.8$ to about 24.5-percent $\bar{c}$ at $M = 1.0$. There was a slight shift rearward at $M = 1.3$ and then a smooth forward movement to about 19-percent $\bar{c}$ at $M = 1.65$.

2. Pitching effectiveness C_{m_δ} of the canard was maintained throughout the flight speed range, the supersonic values being somewhat higher than the subsonic, and lift effectiveness C_{L_δ} was essentially zero.

3. The model encountered abrupt trim changes in angle of attack and lift coefficient between Mach numbers 0.8 and 1.0, the change being associated with variations in C_{m_0}, C_{m_δ}, and center-of-pressure travel in this speed range. The values of α_0 and C_{m_0} were fairly constant in the subsonic and supersonic range with an increase occurring in the region of $M = 0.9$ to $M = 1.0$.

4. Duct total pressure was about 7 percent less than normal-shock recovery at $M = 1.7$ and about 2 percent less at $M = 1.0$. The internal drag of the ducts was a small portion of the total drag. For the angle-of-attack range covered, there was no appreciable variation of duct total pressure with angle of attack.

5. Minimum drag coefficient was of the order of 0.02 subsonically and 0.04 supersonically. The drag-rise Mach number was approximately 0.9. Base drag was quite small subsonically, but was about 25 percent of the minimum drag supersonically.

6. Comparison of the flight data with existing wind-tunnel data for the same configuration in general showed good agreement. It was shown that the differences between wind-tunnel and flight lift-curve

slopes were due in greater part to aeroelastic effects on the wing and
flexibility effects of the fuselage of the flight model.

Langley Aeronautical Laboratory,
       National Advisory Committee for Aeronautics,
               Langley Field, Va.

Aleck C. Bond

Aleck C. Bond
Aeronautical Research Scientist

Andrew G. Swanson

Andrew G. Swanson
Aeronautical Research Scientist

Approved: *Joseph A. Shortal*
                    Joseph A. Shortal
          Chief of Pilotless Aircraft Research Division

ecc

REFERENCES

1. Mitchell, Jesse L., and Peck, Robert F.: An NACA Vane-Type Angle-of-
   Attack Indicator for Use at Subsonic and Supersonic Speeds, NACA
   RM L9F28a, 1949.

2. Gillis, Clarence L., Peck, Robert F., and Vitale, A. James: Preliminary
   Results From a Free-Flight Investigation at Transonic and Supersonic
   Speeds of the Longitudinal Stability and Control Characteristics of
   an Airplane Configuration With a Thin Straight Wing of Aspect
   Ratio 3. NACA RM L9K25a, 1950.

3. Vitale, A. James: Effects of Wing Elasticity on the Aerodynamic Char-
   acteristics of an Airplane Configuration Having 45° Sweptback Wings
   as Obtained from Free-Flight Rocket-Model Tests at Transonic Speeds.
   NACA RM L52L30, 1953.

4. De Young, John, and Harper, Charles W.: Theoretical Symmetric Span
   Loading at Subsonic Speeds for Wings Having Arbitrary Plan Form.
   NACA Rep. 921, 1948.

5. Pfyl, Frank A.: Wind-Tunnel Investigation of the Aerodynamic Character-
   istics of a 0.07-Scale Model of the North American MX-770 Missile.
   NACA RM SA52E07, U. S. Air Force, 1952.

6. Beilock, M.: Aerodynamic Analysis of the RTV-A-5 and NAVAHO Series
   Free-Flight Rocket-Booster Models. Rep. No. AL-1248, North American
   Aviation, Inc., Apr. 12, 1951.

7. Weight Control Section: Weight, Balance, and Moment of Inertia of
   the RTV-A-5 Free Flight Model. Rep. No. NA-51-409, North American
   Aviation, Inc., Mar. 20, 1951.

8. Gillis, Clarence L., and Chapman, Rowe, Jr.: Summary of Pitch-
   Damping Derivatives of Complete Airplane and Missile Configurations
   As Measured in Flight at Transonic and Supersonic Speeds. NACA
   RM L52K20, 1953.

9. Dryer, Murray, and Beke, Andrew: Performance Characteristics of a
   Normal-Shock Side Inlet Located Downstream of a Canard Control Sur-
   face at Mach Numbers of 1.5 and 1.8. NACA RM E52F09, 1952.

10. Cortright, Edgar M., Jr., and Schroeder, Albert H.: Investigation
    at Mach Number 1.91 of Side and Base Pressure Distributions Over
    Conical Boattails Without and With Jet Flow Issuing From Base.
    NACA RM E51F26, 1951.

TABLE I.- WING AIRFOIL ORDINATES

[Stations and ordinates given in percent of local chord.
Upper ordinate equals lower ordinate.]

Wing root		87.26 percent semispan
Station	Ordinate	Ordinate
0	0	0
.5	.216	.460
1.25	.325	.690
2.5	.433	.920
5	.597	1.265
7.5	.723	1.533
10	.823	1.744
15	1.004	2.127
20	1.130	2.395
25	1.242	2.625
30	1.312	2.780
40	1.403	2.970
45	1.420	3.000
50	1.411	2.989
55	1.385	2.932
60	1.329	2.817
70	1.095	2.318
80	.796	1.648
90	.502	.996
95	.351	.671
100	.203	.345
L.E. radius = 0.020 in.		L.E. radius = 0.020 in.

TABLE II.- CANARD AIRFOIL ORDINATES

Stations and ordinates given in percent of local chord.
Upper ordinate equals lower ordinate.

Station	Ordinate
0	0
.5	.393
.75	.464
1.25	.578
2.5	.764
5	1.050
7.5	1.270
10	1.475
15	1.770
20	2.000
25	2.185
30	2.320
40	2.480
45	2.500
50	2.495
60	2.350
70	1.935
Straight line to trailing edge	
100	.035
L.E. radius = 1.55 percent local chord	

TABLE III.- VERTICAL-TAIL ORDINATES

[Stations and ordinates given in percent of local chord.
Upper ordinates equals lower ordinates.]

| Root chord (10.800 in. from tip) | | Tip chord |
Station	Ordinate	Ordinate
0	0	0
.75	.102	.143
1.25	.118	.190
2.5	.269	.309
5	.501	.547
10	.918	.952
15	1.290	1.309
20	1.614	1.618
25	1.883	1.904
30	2.106	2.118
40	2.403	2.404
50	2.496	2.500
60	2.403	2.404
70	2.106	2.118
75	1.883	1.904
81	1.549	1.571
Straight line to trailing edge		
100	.390	.428
L.E. radius = 0.004 in.		

WING

Aspect ratio	1.87
Area (including fuselage)	6.12 sq ft
Area (exposed)	3.33 sq ft
Dihedral	0.0 deg
Incidence	-2.0 deg
M.A.C.	26.94 in.

CANARD

Aspect ratio (projected span and area)	1.78
Area (total)	1.08 sq ft
Area (projected exposed)	0.56 sq ft
Dihedral	15.0 deg
M.A.C.	7.87 in.
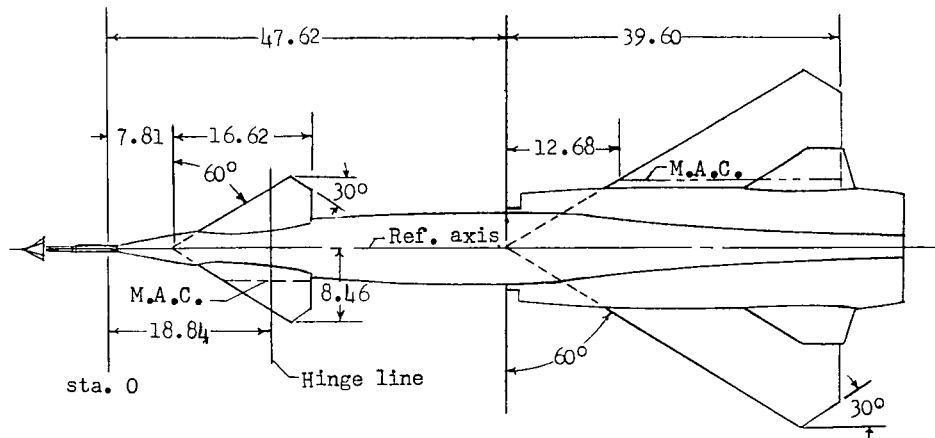
VERTICAL TAIL

Area (total exposed)	1.19 sq ft
Dihedral	65.0 deg
Incidence	0.0 deg
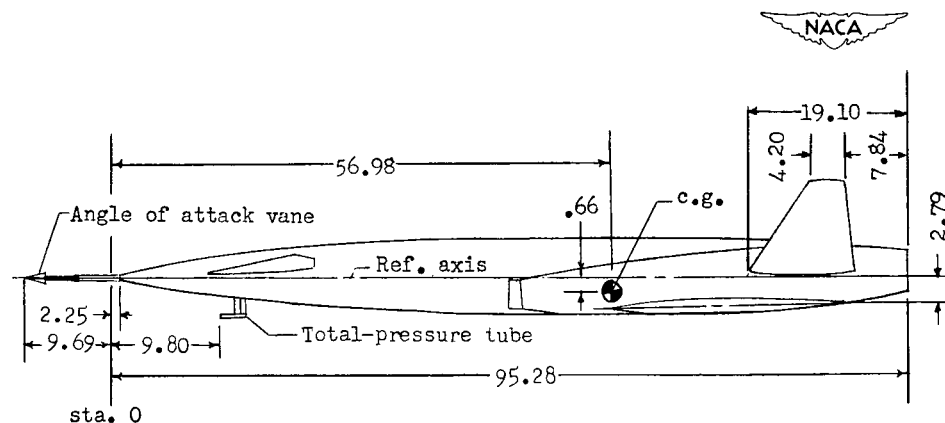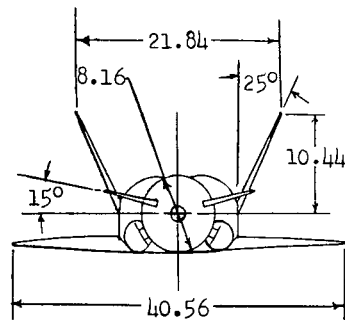
Figure 1.- General arrangement of the model. All dimensions in inches.
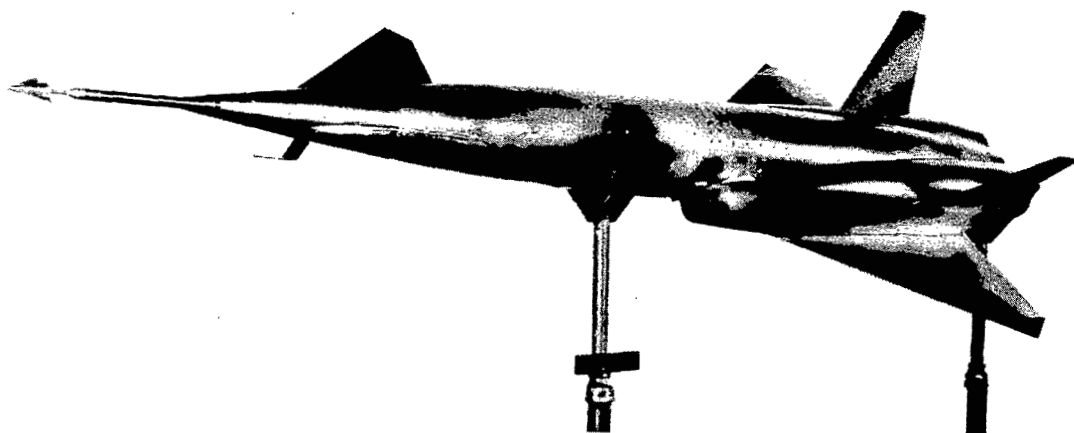
(a) Three-quarter front view. L-75488.1
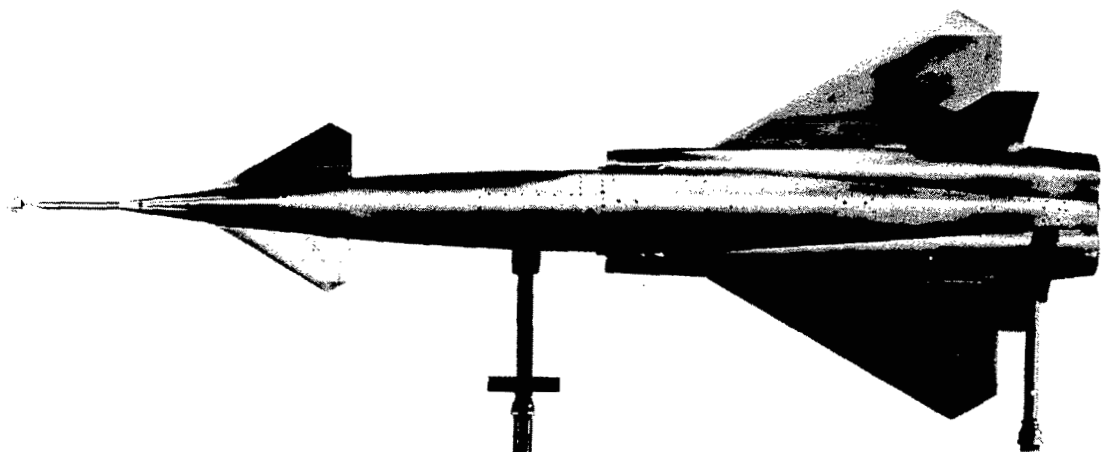
(b) Top view. L-77598.1

Figure 2.- Photographs of model.
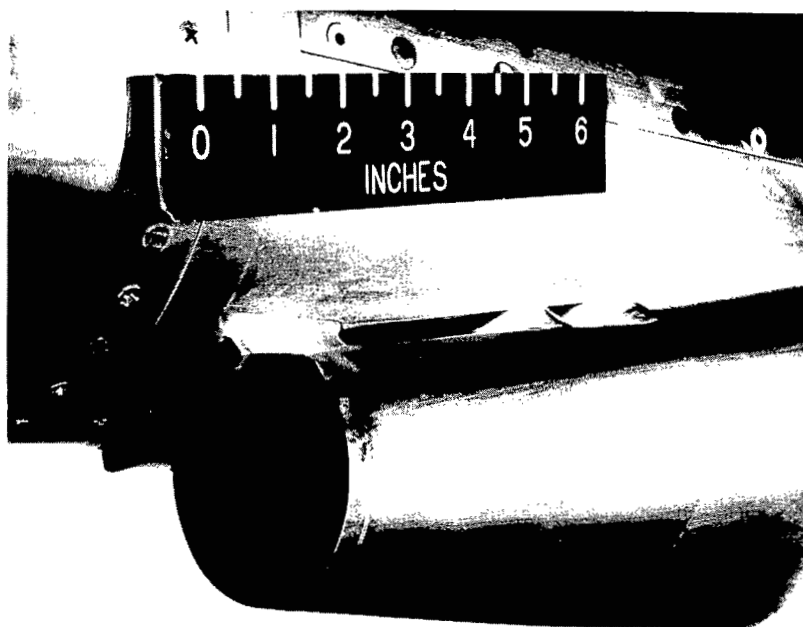
(a) Three-quarter front view. L-75491
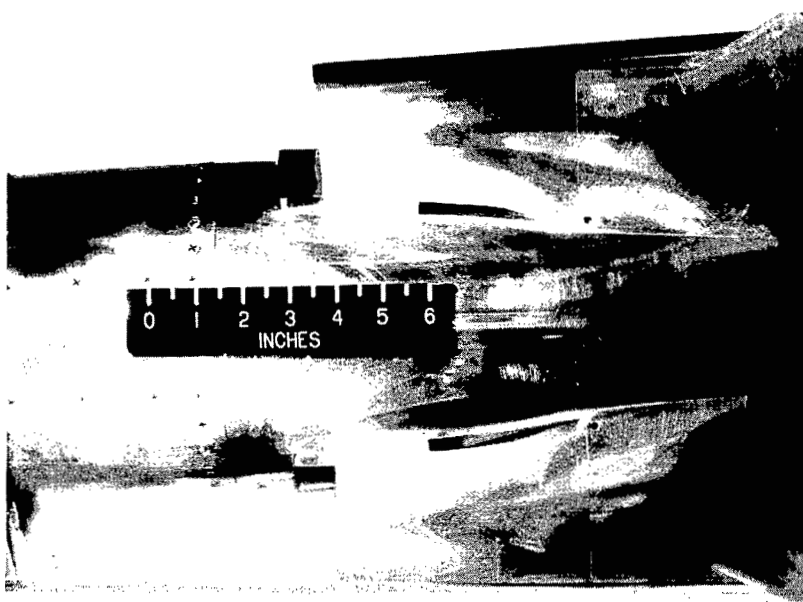
(b) Bottom view. L-75492

Figure 3.- Inlet and boundary-layer bleed details.
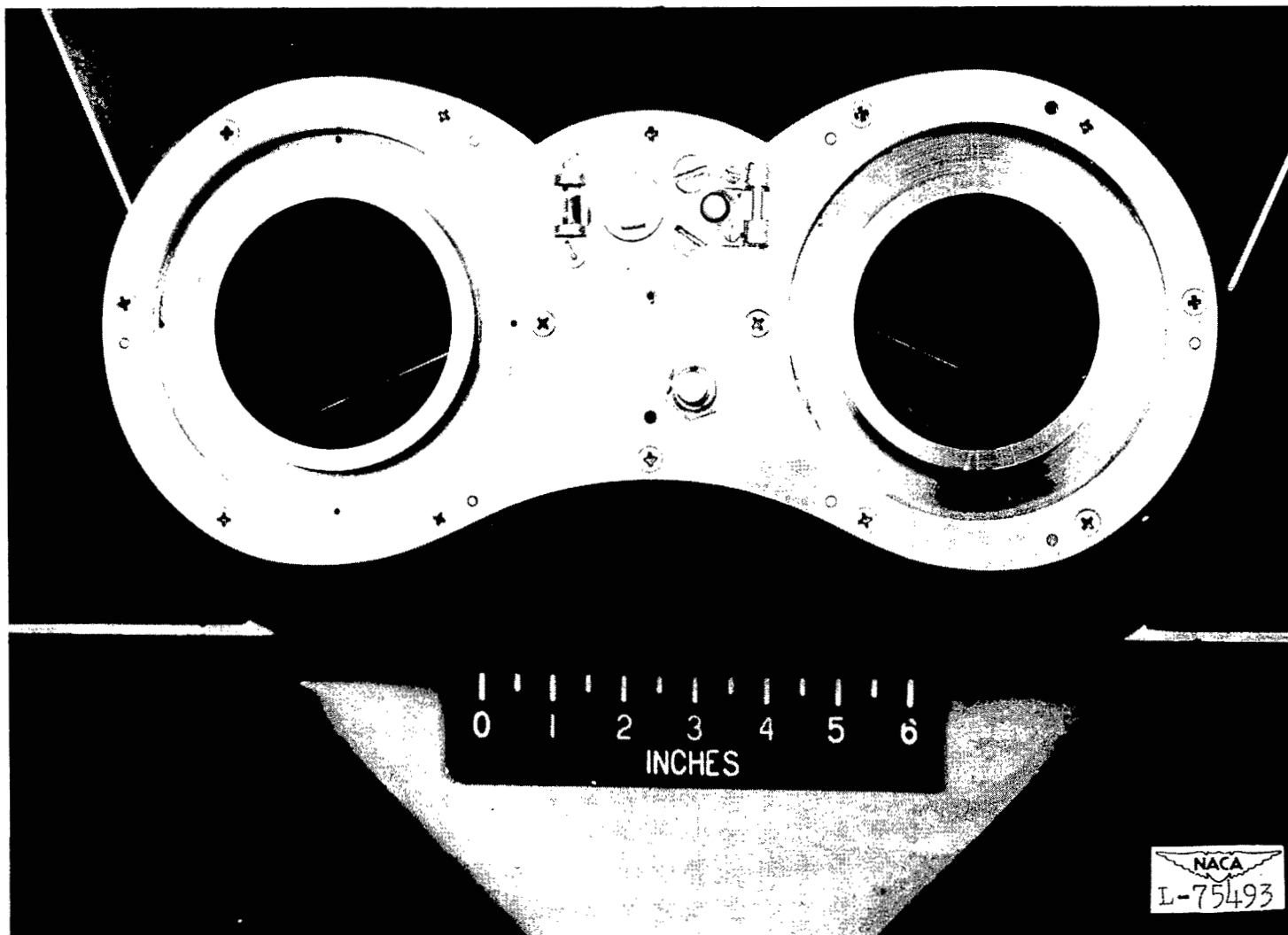
Figure 4.- Duct exit and base details.

.88

2.55

.60

3.81

3.40
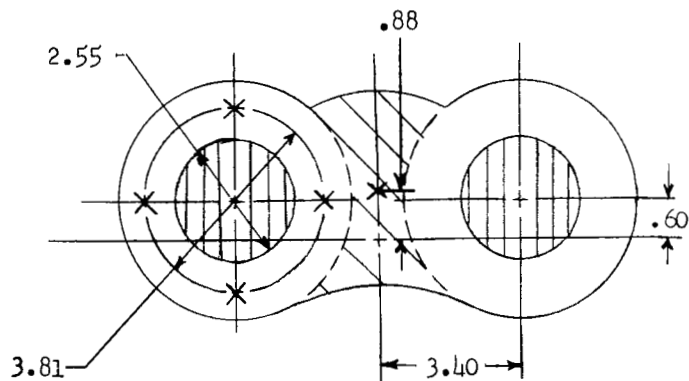
Assumed area of influence of base pressures measured by manifolded orifices, 29.056 sq in.

Assumed area of influence of base pressures measured by center orifice, 8.770 sw sq in.

Jet exit area, 10.214 sq in.

X Location of pressure orifices

8.16 diam.

Ref. axis

6°

Boundary layer bleed

4 diam.

2°

Static pressure orifice

Total pressure rake (shown rotated from true position 125° clockwise as viewed from after end).

sta. 86.75

sta. 94.57

NACA
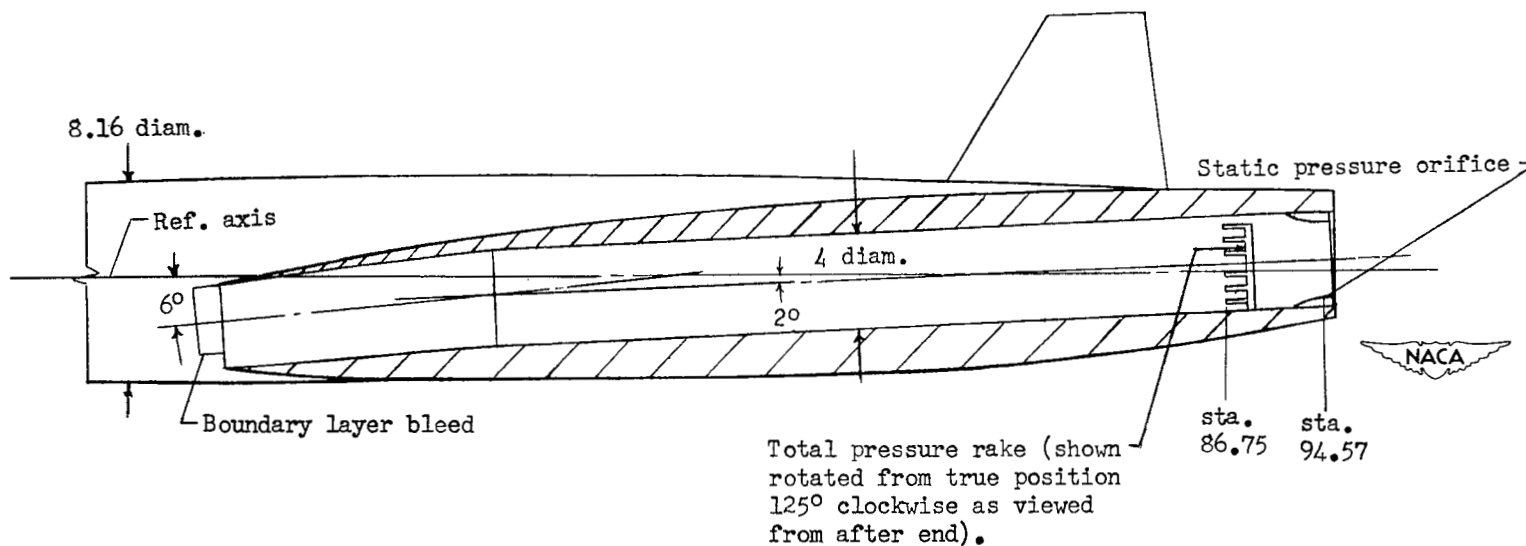
Figure 5.- Duct and base details. All dimensions in inches.
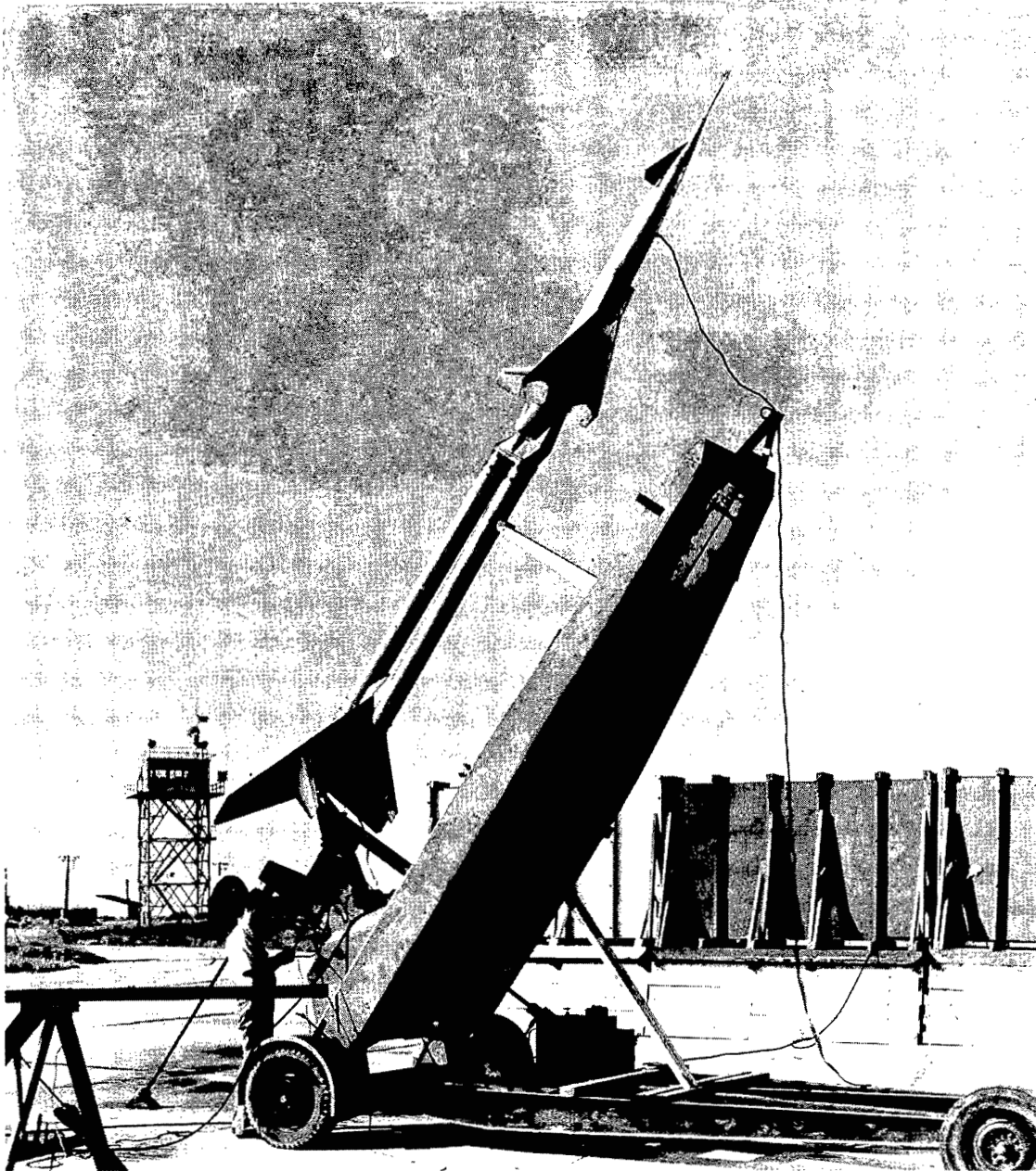
Figure 6.- Model on launcher. L-75612
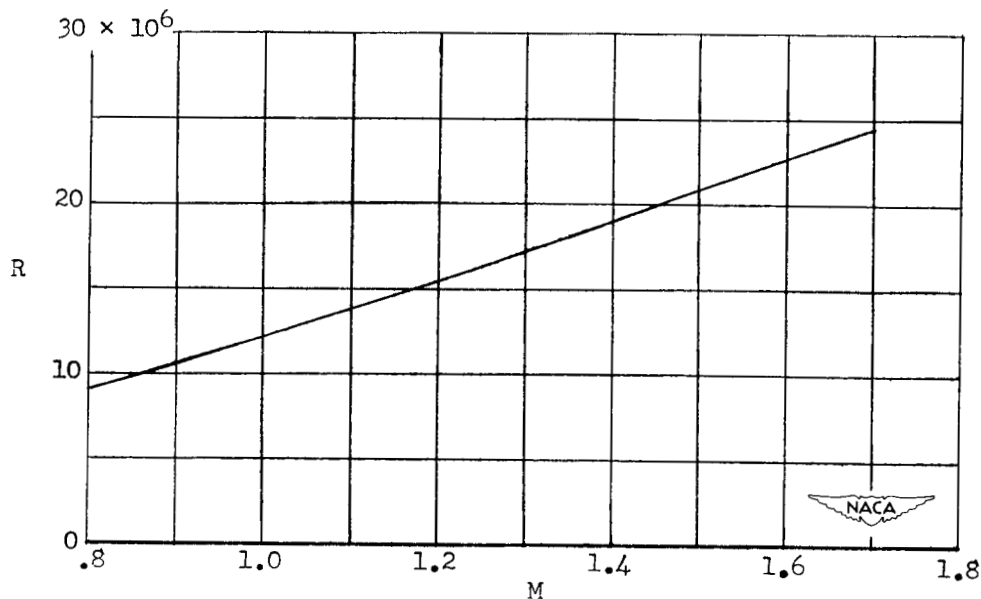
Figure 7.- Test Reynolds number based on wing mean aerodynamic chord.
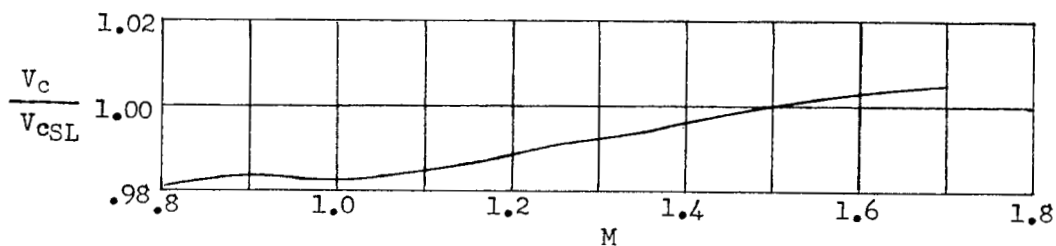
(a) Acoustic-velocity ratio.
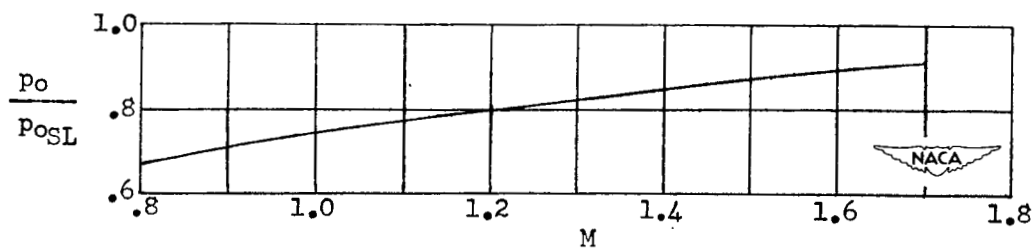
(b) Static-pressure ratio.

Figure 8.- Atmospheric data.
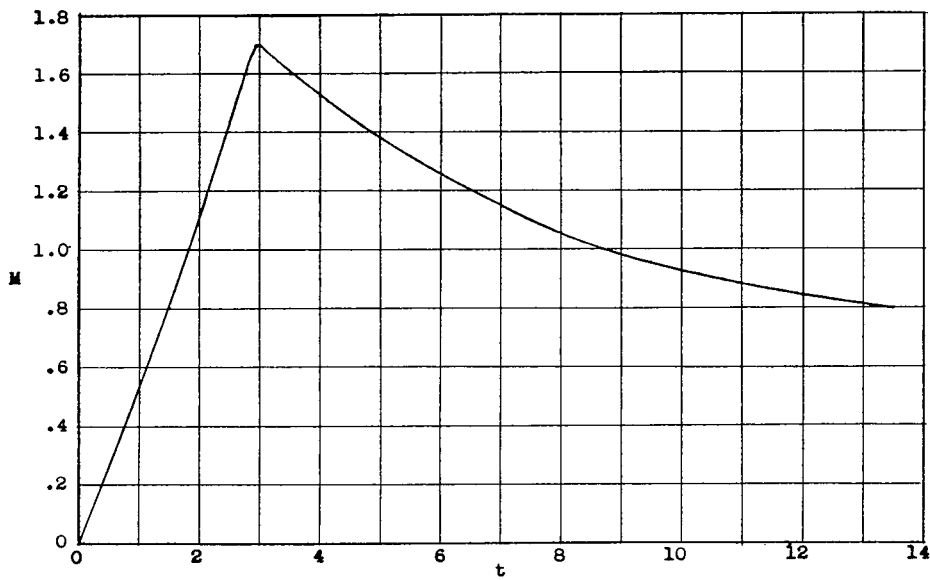
(a) Variation of Mach number with time.
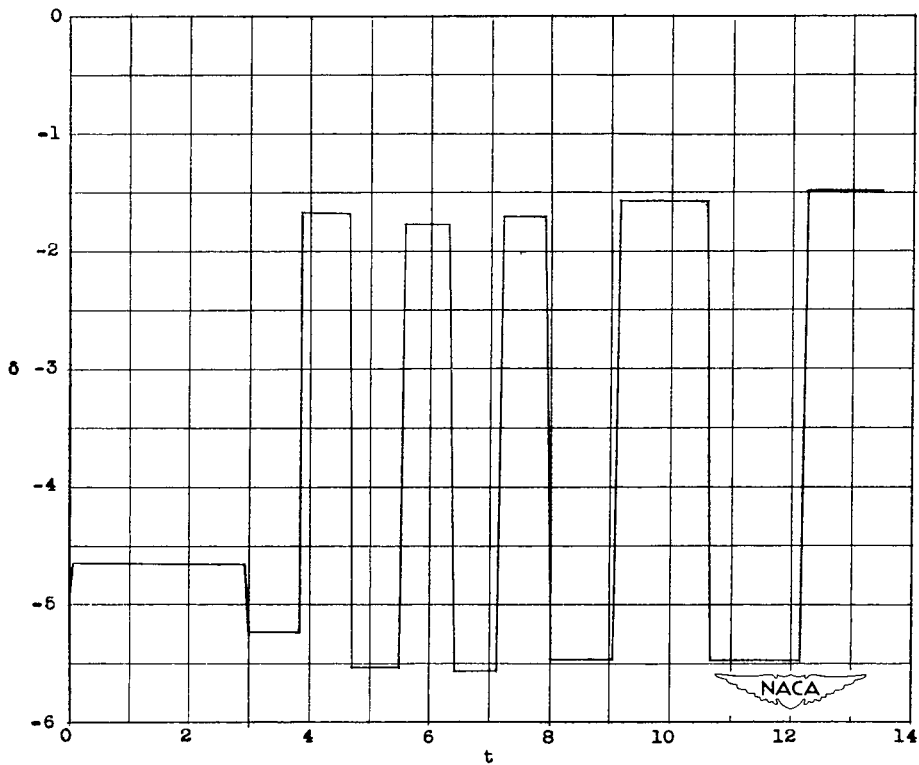
(b) Variation of canard position with time.

Figure 9.- Canard deflection angle and Mach number variation with time.
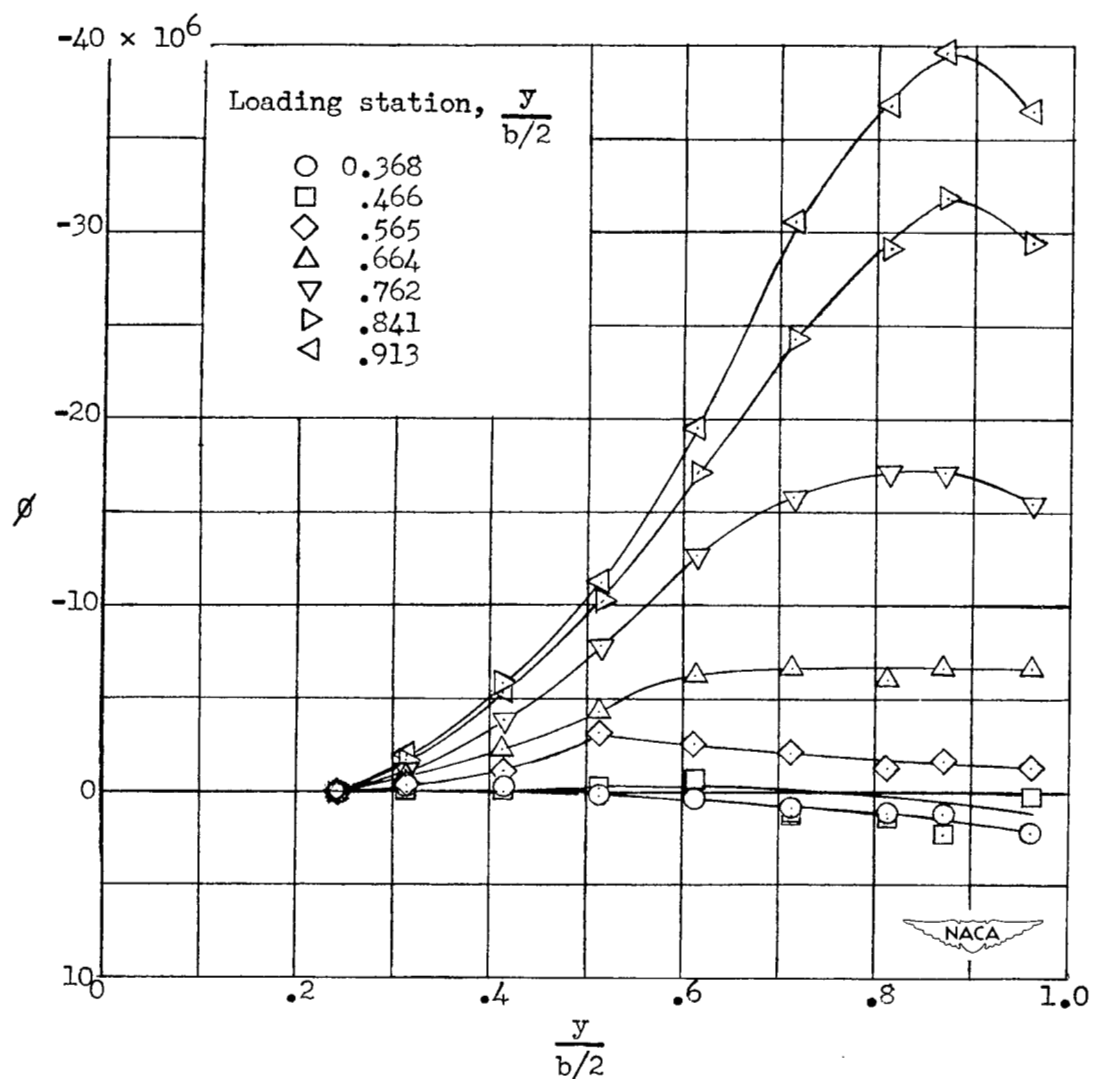
Figure 10.- Twist in the free-stream direction per unit load applied at various stations along the span of the wing on the 50-percent chord line.
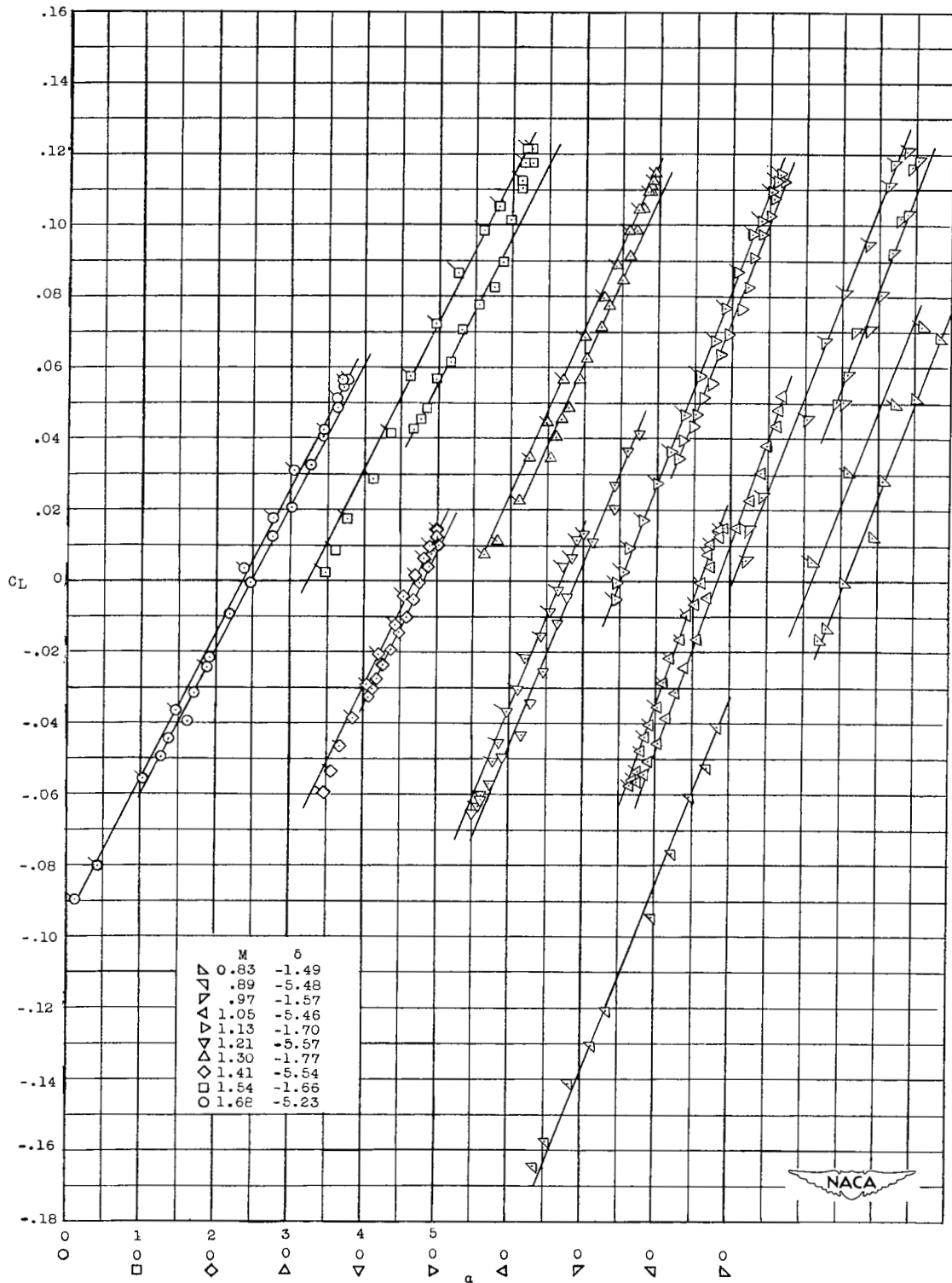
Figure 11.- Variation of lift coefficient with angle of attack. Flagged
symbols denote positive values of dα/dt.
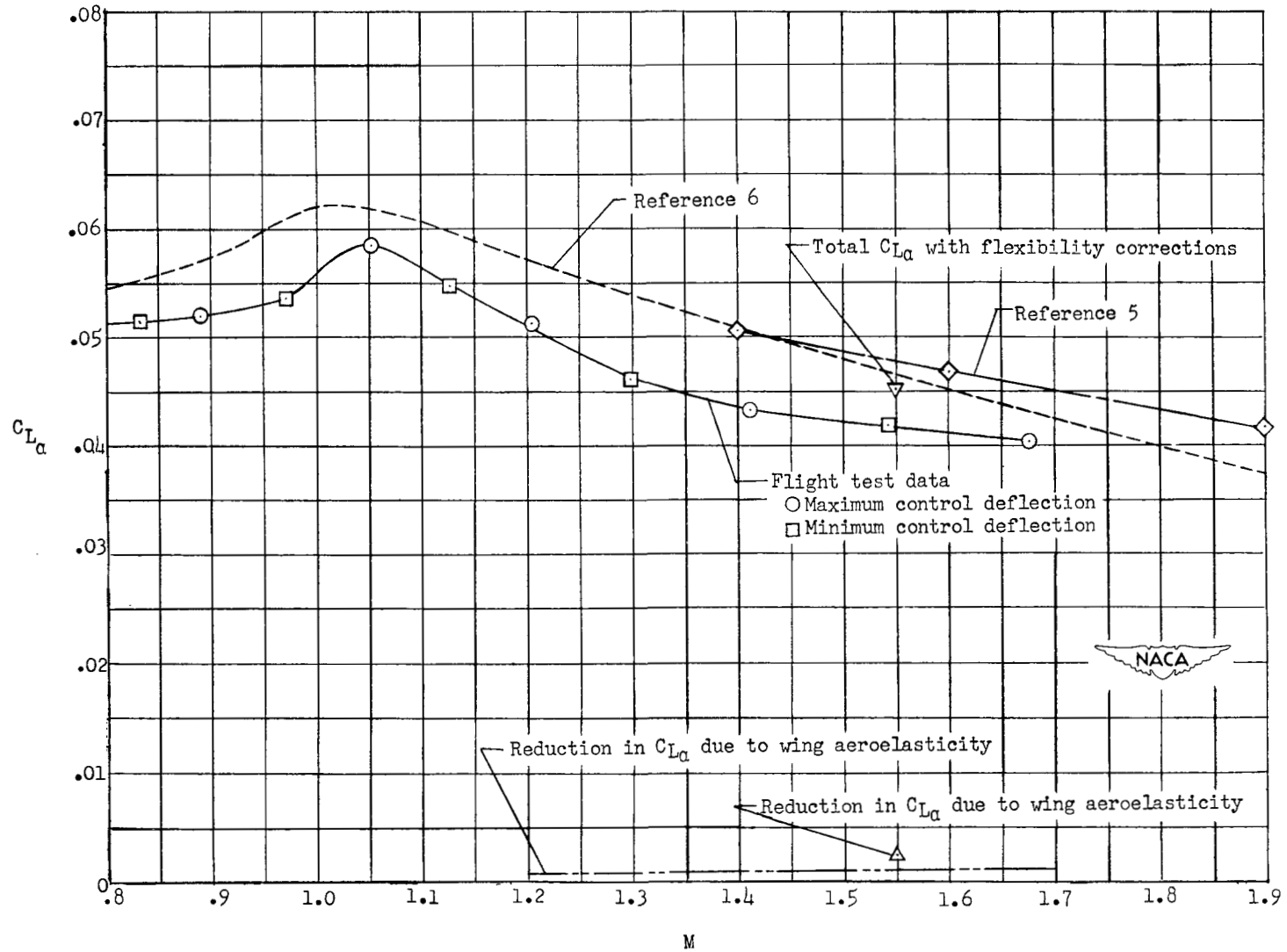
Figure 12.- Lift-curve slope.
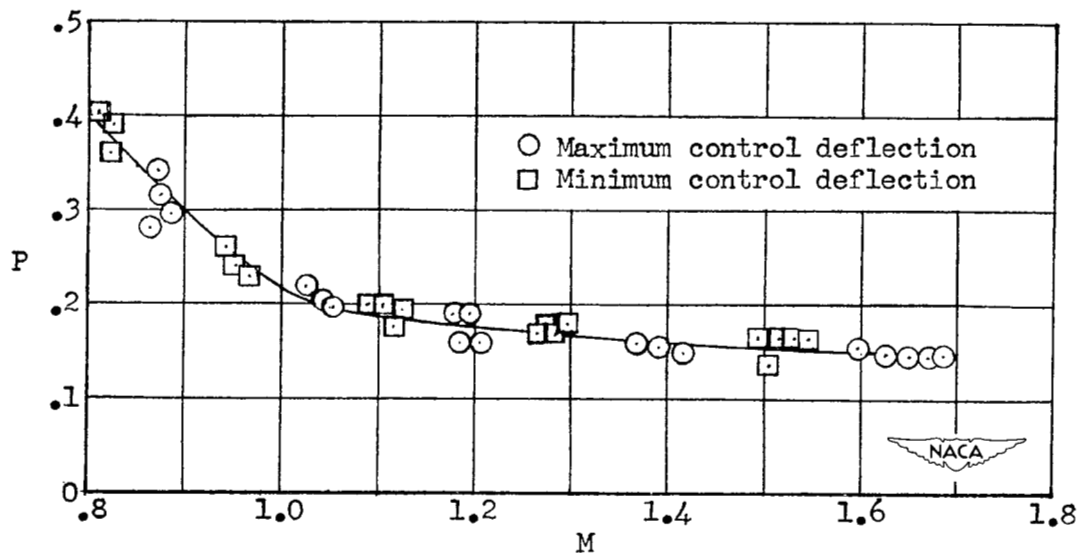
Figure 13.- Period of pitch oscillations.
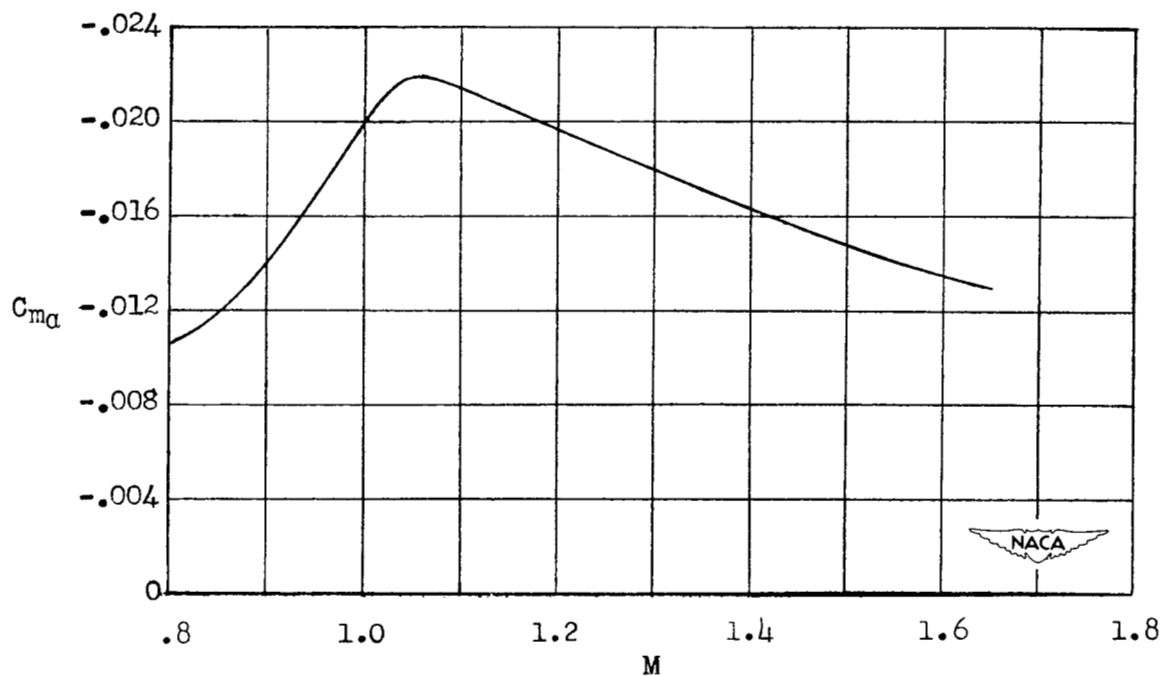
Figure 14.- Longitudinal-stability parameter C_{m_α}.
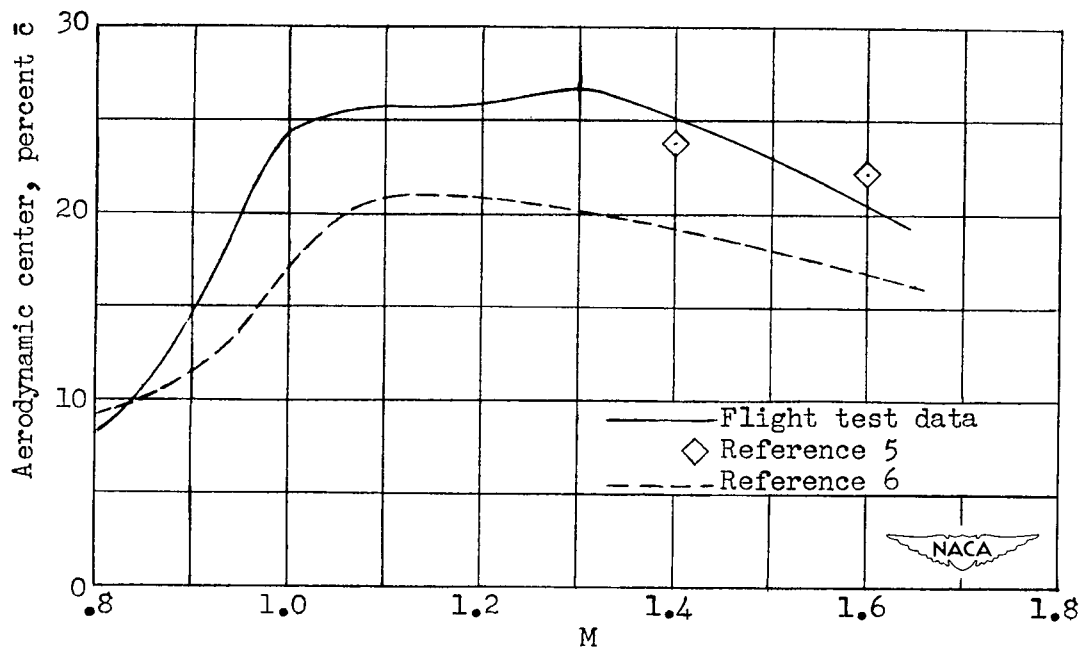
Figure 15.- Aerodynamic-center position.
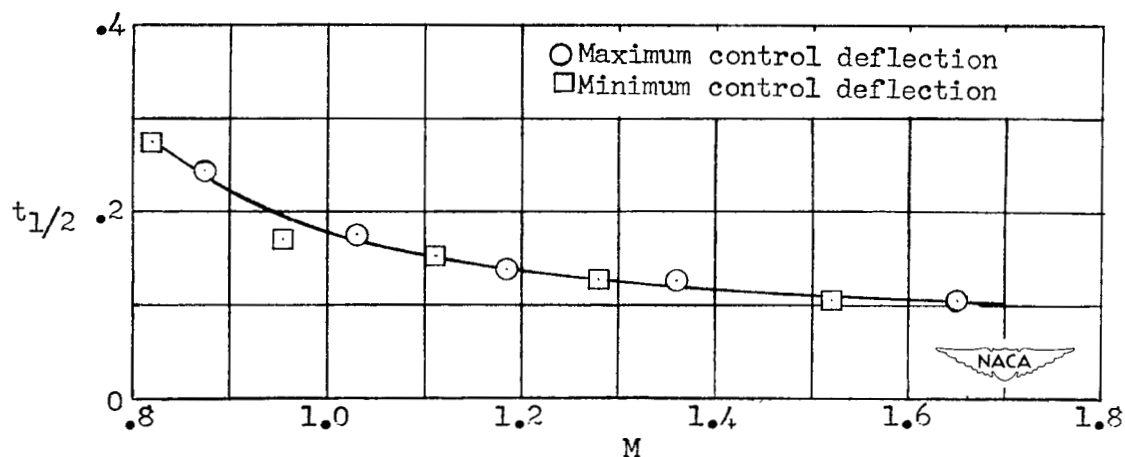
Figure 16.- Time to damp to one-half amplitude.
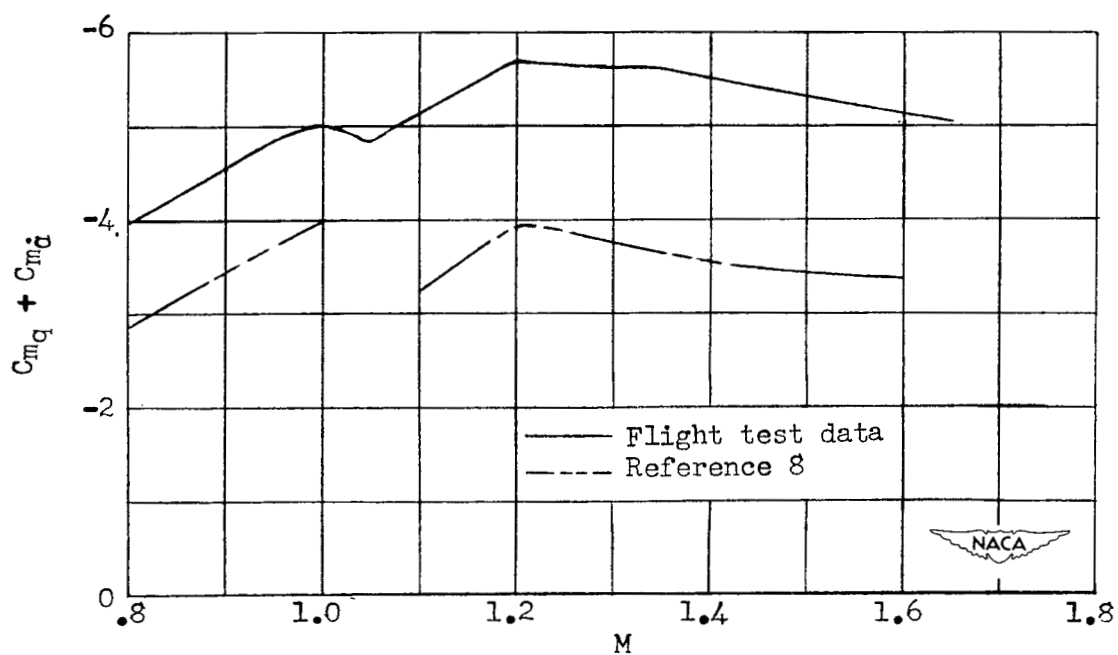
Figure 17.- Pitching-moment damping derivative $C_{m_q} + C_{m_{\dot{\alpha}}}$.
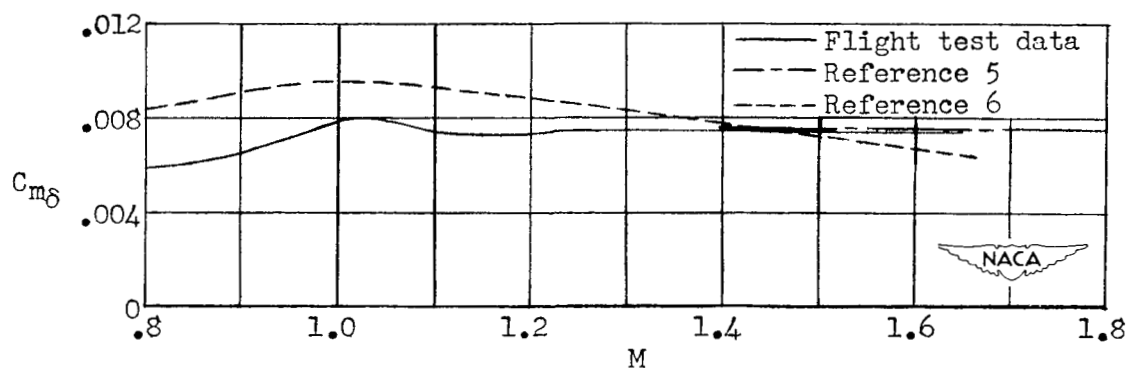
Figure 18.- Effectiveness of canard in producing pitching moment.
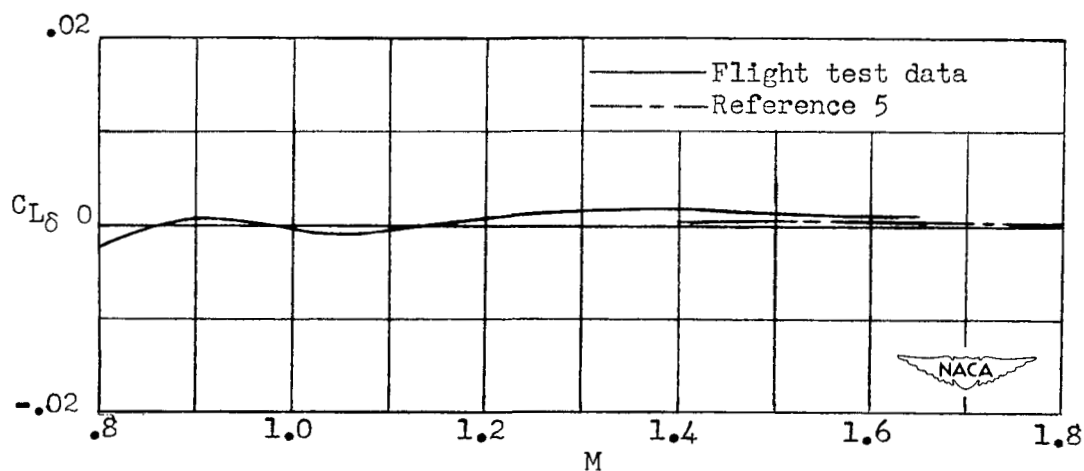
Figure 19.- Effectiveness of canard in producing lift.
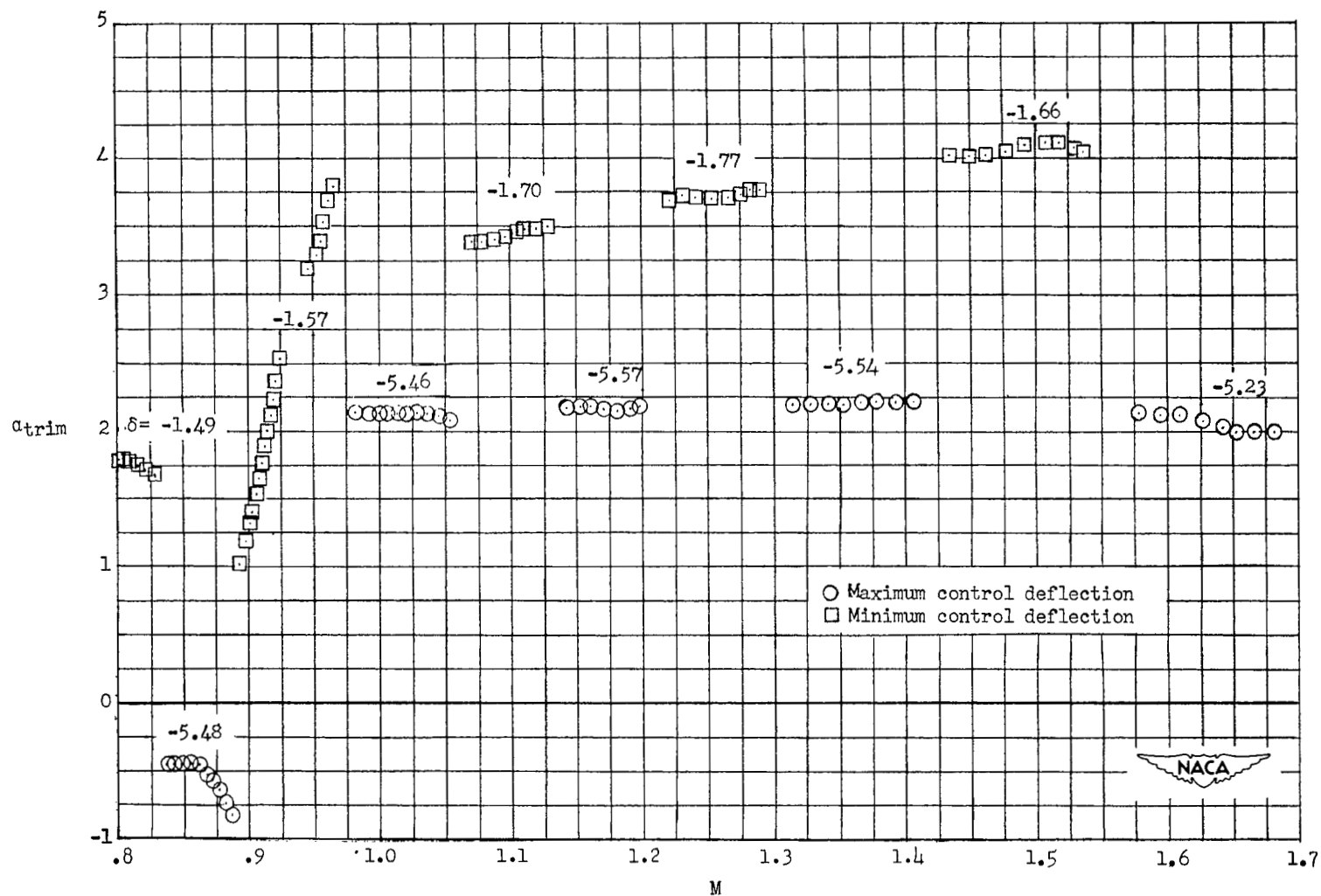
(a) Angle of attack.

Figure 20.- Trim data for varying control position.
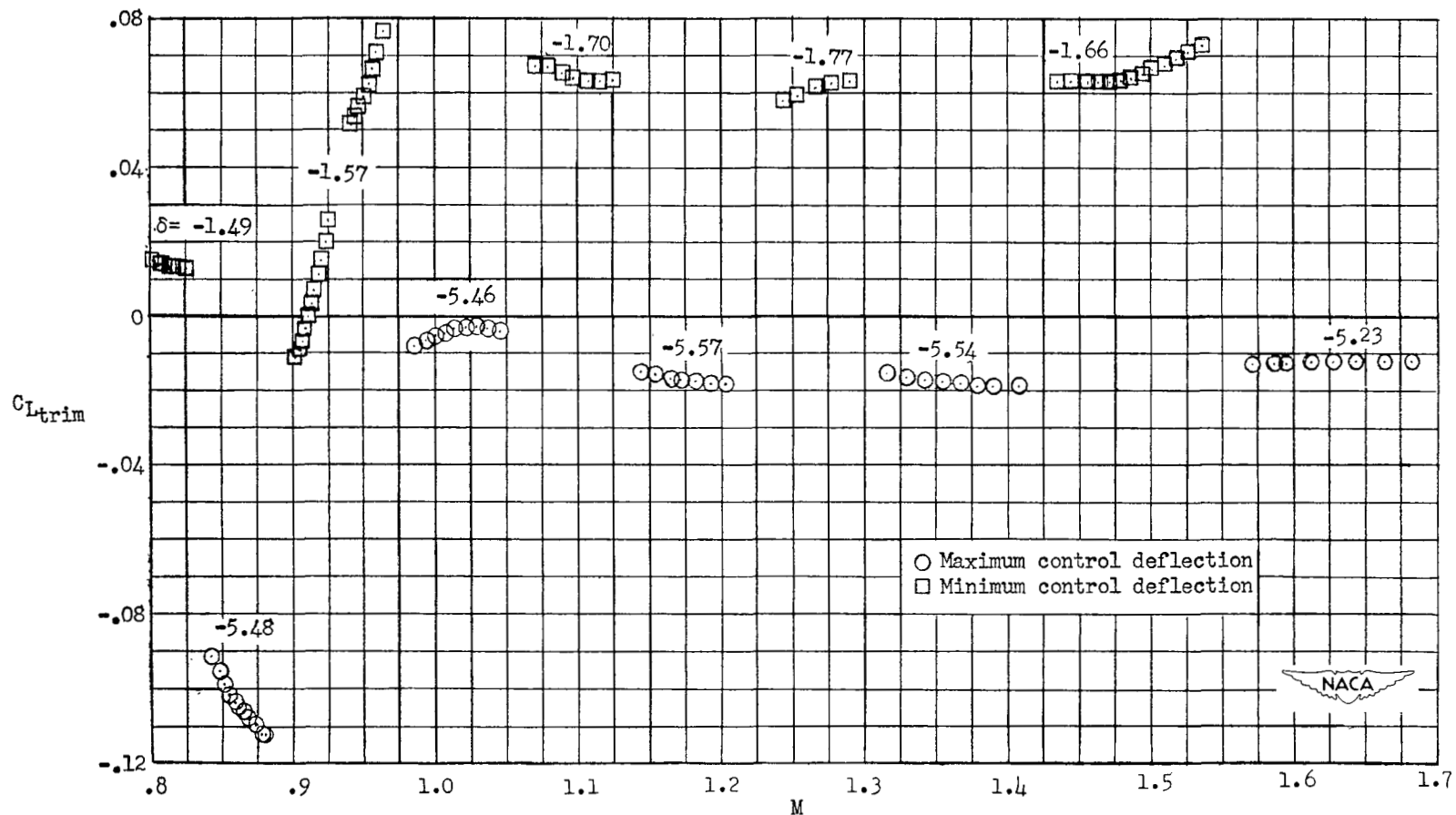
(b) Lift coefficient.

Figure 20.- Concluded.
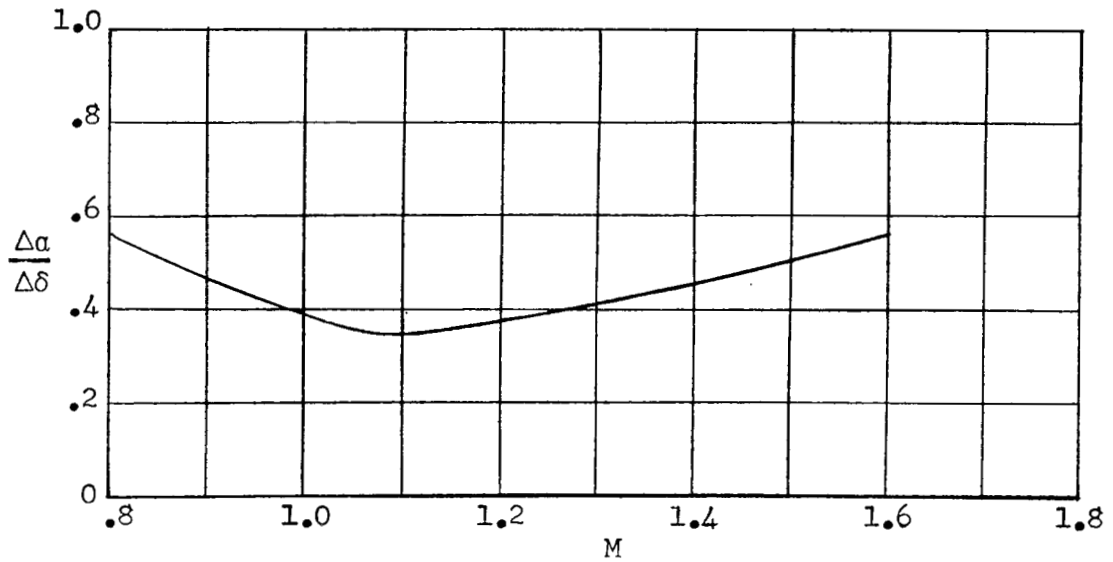
(a) Angle of attack.
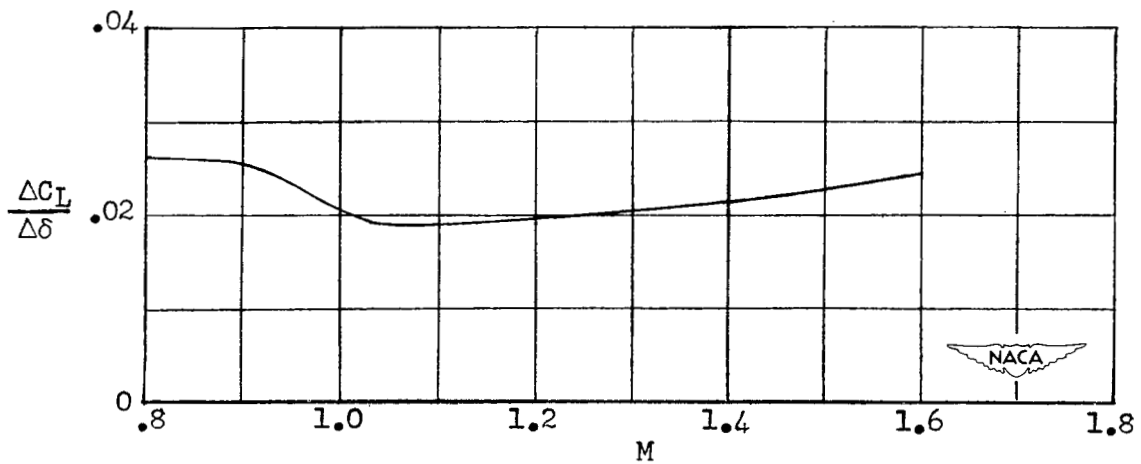
(b) Lift coefficient.

Figure 21.- Change in trim parameters per unit control deflection.
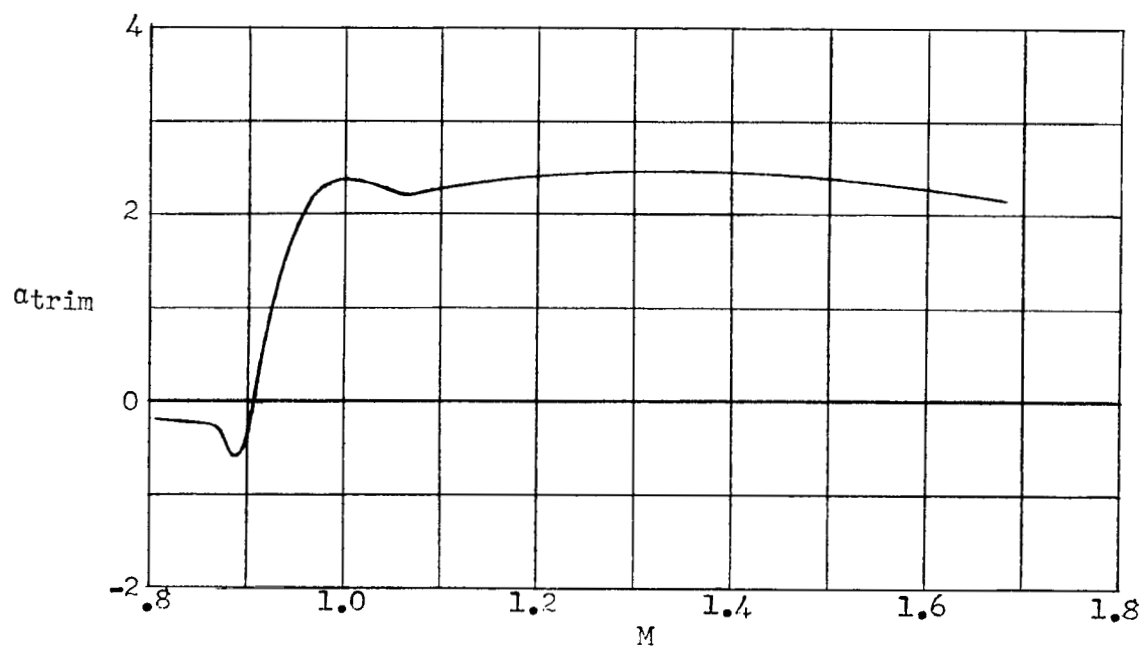
(a) Angle of attack.
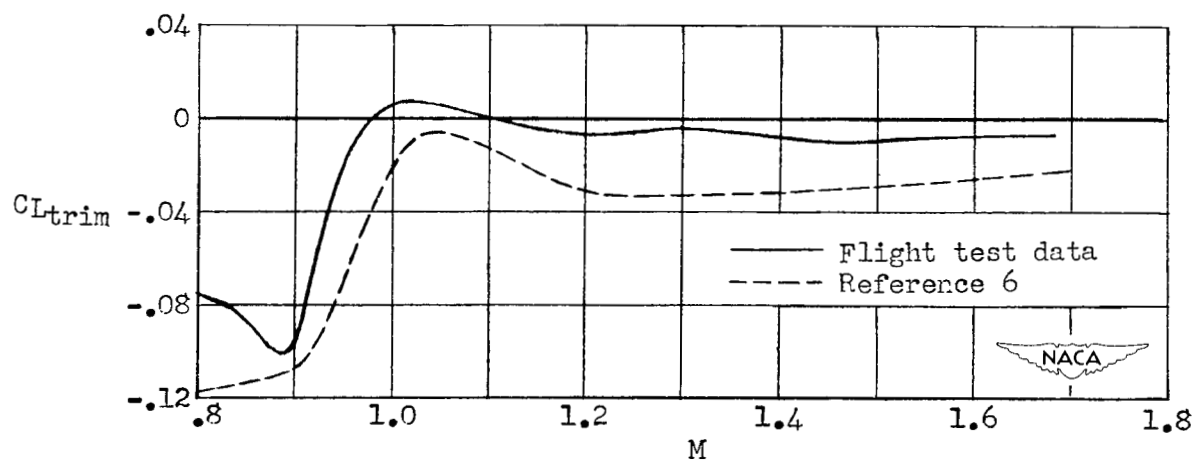
(b) Lift coefficient.

Figure 22.- Trim data for constant control position. $\delta = -5°$.
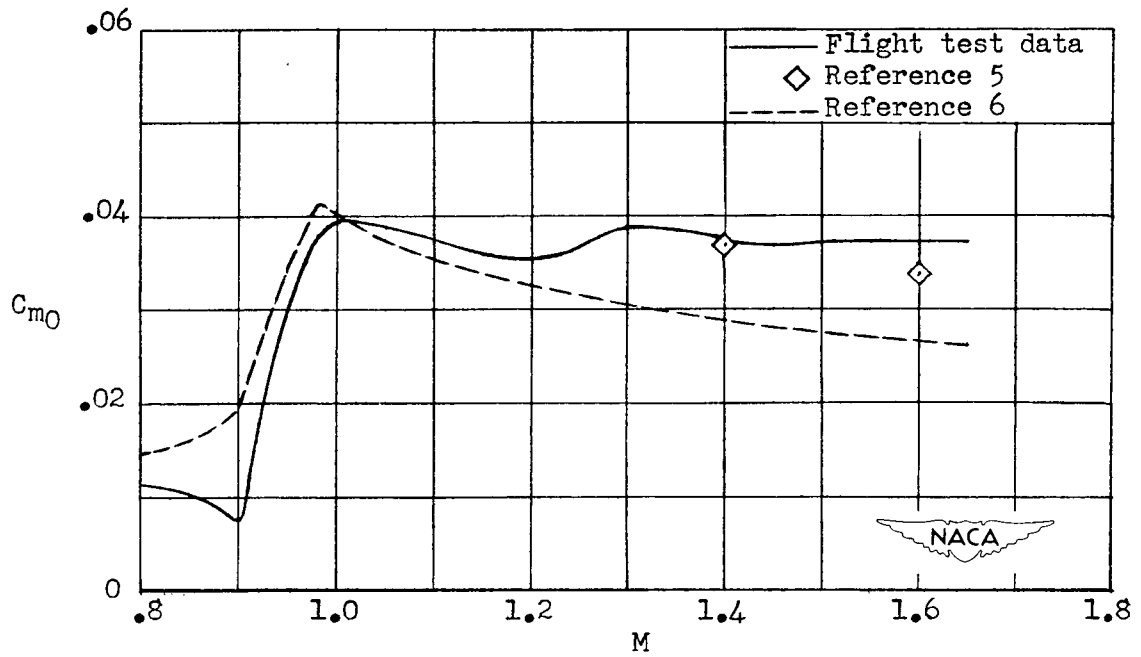
Figure 23.- Pitching-moment coefficient at zero lift and zero control deflection.
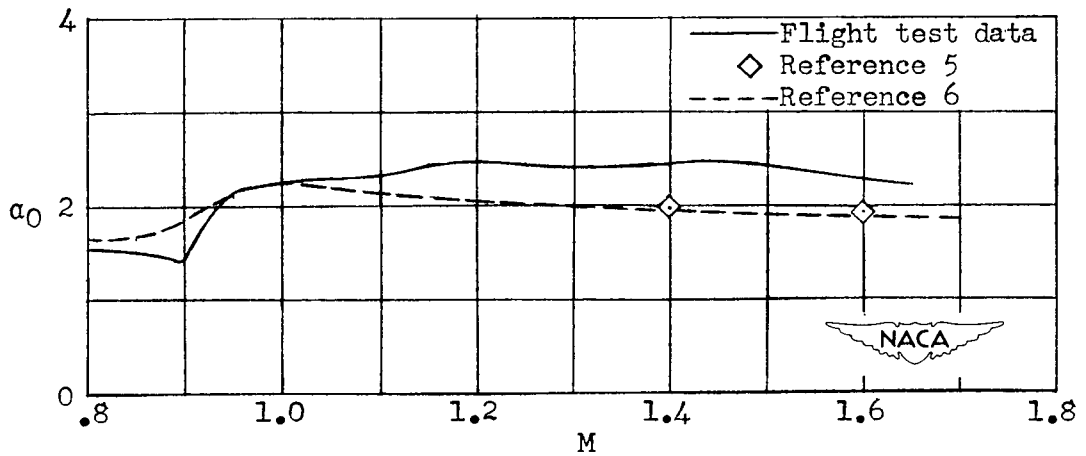
Figure 24.- Angle of attack at zero lift and zero control deflection.
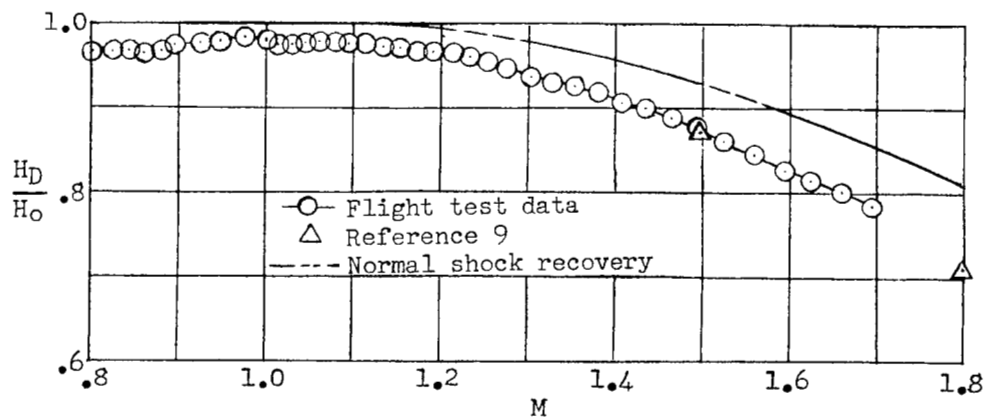
(a) Total-pressure recovery.
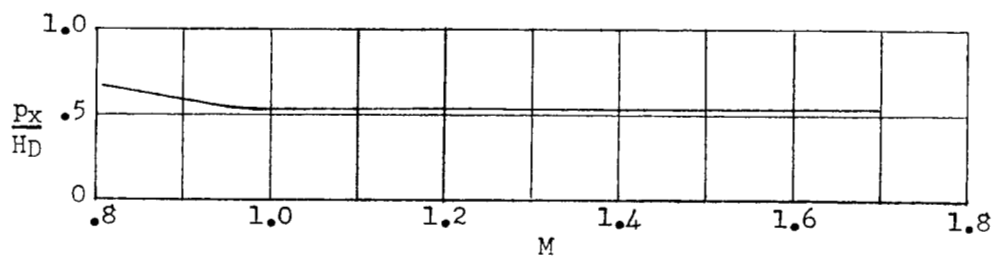
(b) Jet-exit pressure ratio.
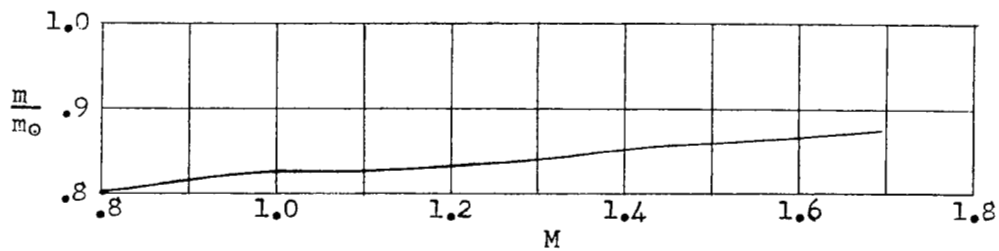
(c) Mass-flow ratio.
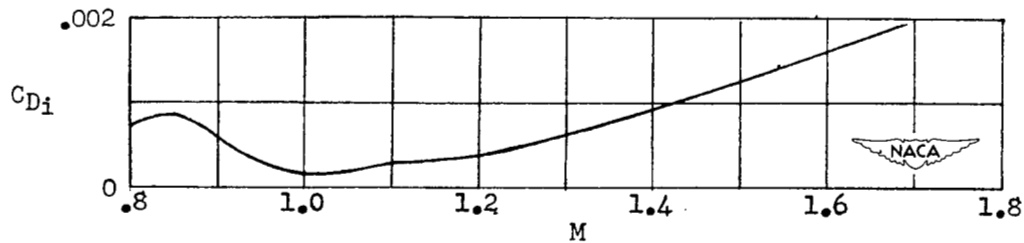
(d) Total internal-drag coefficient.

Figure 25.- Duct-performance data.
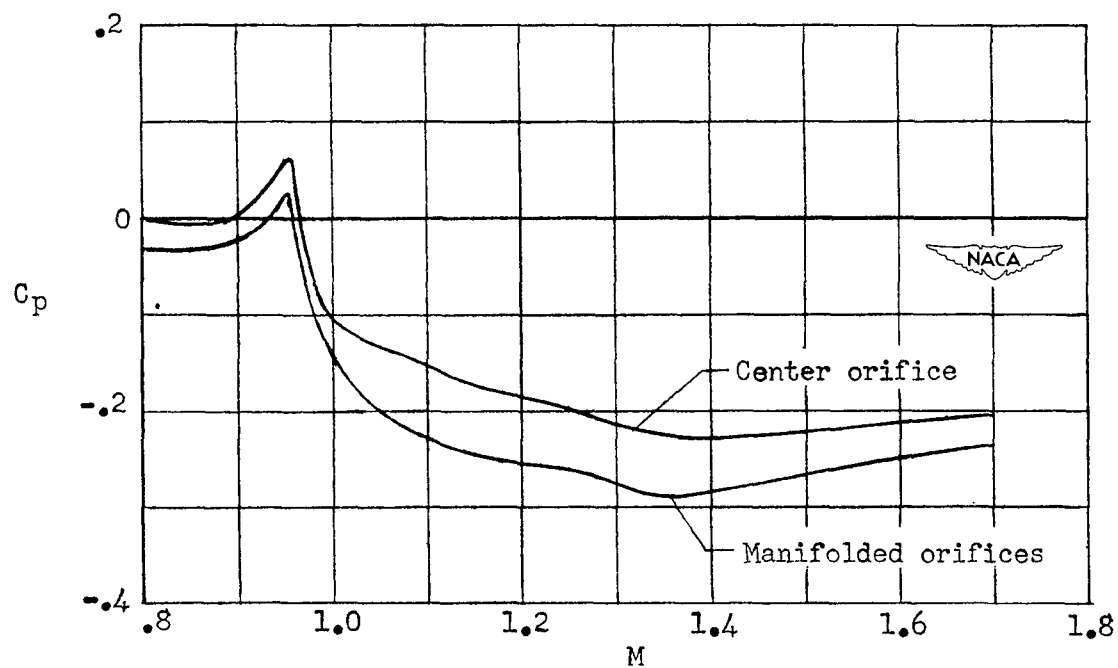
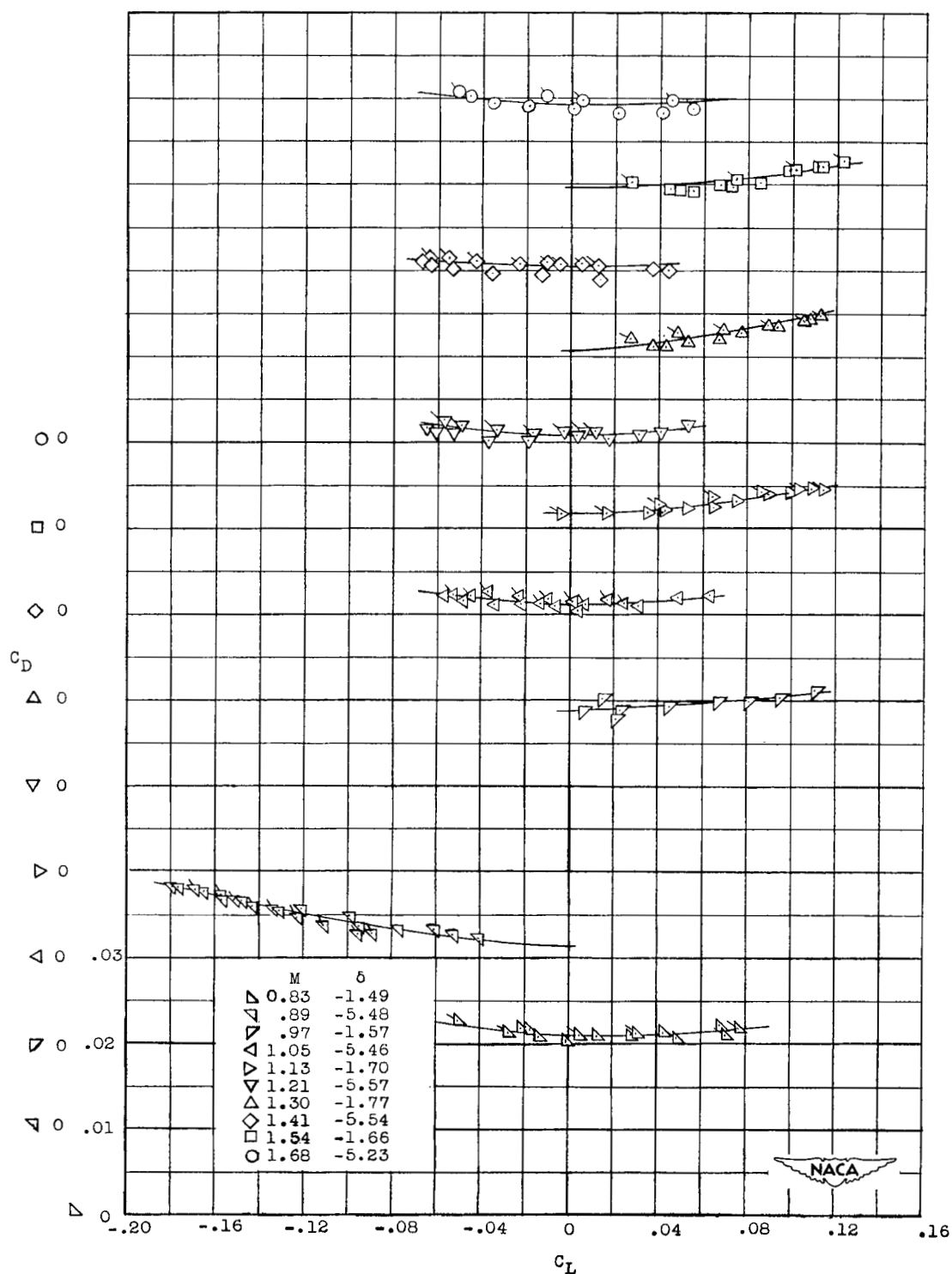Figure 26.- Base pressure coefficient.

Figure 27.- Variation of total drag coefficient with lift coefficient.
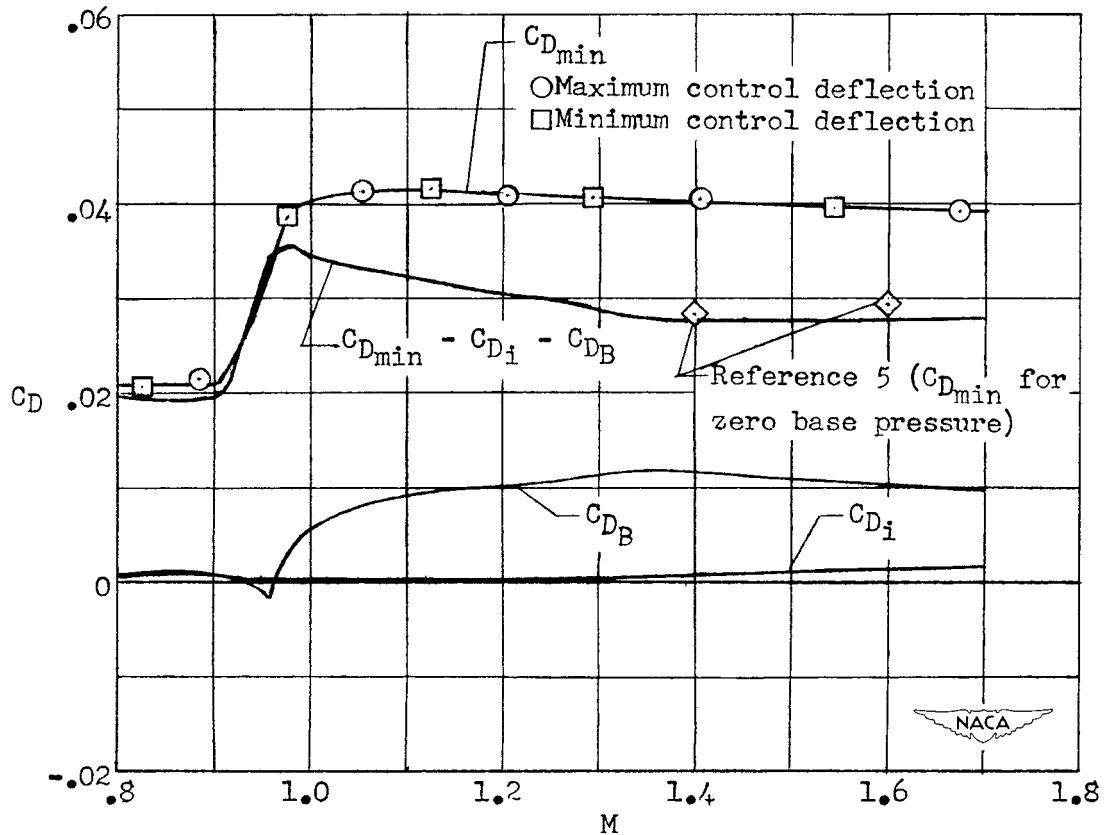Flagged symbols denote positive values of dα/dt.

Figure 28.- Variation of drag coefficients with Mach number.